Goda, K., Yasuda, T., Mori, N., & Maruyama, T. (2016). New Scaling Relationships of Earthquake Source Parameters for Stochastic Tsunami Simulation. Coastal Engineering Journal, 58(3), [1650010]. DOI: 10.1142/S0578563416500108

World Scientific
www.worldscientific.com

JAPAN SOCIETY OF CIVIL ENGINEERS
COASTAL ENGINEERING COMMITTEE

Coastal Engineering Journal, Vol. 58, No. 3 (2016) 1650010 (40 pages)

DOI: 10.1142/S0578563416500108

New Scaling Relationships of Earthquake Source Parameters for Stochastic Tsunami Simulation

Katsuichiro Goda

Department of Civil Engineering, Queen's School of Engineering, University of Bristol, Queen's Building, University Walk, Bristol, BS8 1TR, UK
katsu.goda@bristol.ac.uk

Tomohiro Yasuda

Faculty of Environmental and Urban Engineering, Kansai University, 3-3-35 Yamate-cho, Suita, Osaka 564-8680, Japan

Nobuhito Mori and Takuma Maruyama

Disaster Prevention Research Institute, Kyoto University, Gokasho, Uji, Kyoto 611-0011, Japan

Received 9 March 2016
Accepted 26 July 2016
Published 16 September 2016

New scaling relationships of key earthquake source parameters are developed by uniformly and systematically analyzing 226 finite-fault rupture models from the SRCMOD database (http://equake-rc.info/srcmod/). The source parameters include the fault width, fault length, fault area, mean slip, maximum slip, Box-Cox power, correlation lengths along dip and strike directions, and Hurst number. The scaling relationships are developed by distinguishing tsunamigenic models from non-tsunamigenic models; typically, the former occurs in ocean and has gentler dip angles than the latter. The new models are based on extensive data, including recent mega-thrust events, and thus are more reliable. Moreover,

they can be implemented as multivariate probabilistic models that take into account uncertainty and dependency of the multiple source parameters. The comparison between new and existing models indicates that the new relationships are similar to the existing ones for earthquakes with magnitudes up to about 8.0, whereas the relationships for the fault width and related parameters differ significantly for larger mega-thrust events. An application of the developed scaling relationships in tsunami hazard analysis is demonstrated by synthesizing stochastic earthquake source models in the Tohoku region of Japan. The examples are aimed at providing practical guidance as to how the developed scaling relationships can be implemented in stochastic tsunami simulation. The numerical results indicate that the effects of magnitude scaling of the source parameters and their uncertainties have major influence on the tsunami hazard assessment.

Keywords: Scaling relationship; earthquake source parameter; finite-fault rupture model; tsunamigenic earthquake; stochastic source modeling; tsunami simulation.

1. Introduction

Earthquake source modeling aims at predicting key characteristics of a fault rupture (e.g. geometry and slip distribution) based on past major earthquakes. Typically, results are summarized as empirical scaling relationships [e.g. Wells and Coppersmith, 1994; Somerville *et al.*, 1999; Mai and Beroza, 2000, 2002; Papazachos *et al.*, 2004; Blaser *et al.*, 2010; Leonard, 2010; Strasser *et al.*, 2010; Murotani *et al.*, 2013]. These are essential tools for characterizing earthquake rupture models for future events. They are also useful for defining a range of uncertain earthquake source features in tsunami hazard assessment [Goda *et al.*, 2014, 2015; Fukutani *et al.*, 2015; Mueller *et al.*, 2015]. The uncertainties can be further propagated in tsunami loss estimation to promote effective tsunami risk mitigation decisions [Goda and Abilova, 2016]. For such applications, various parameters need to be specified, including geometry (in accordance with regional seismotectonic setting), slip statistics (mean, maximum, and distribution type), spatial slip distribution, and temporal rupture evolution [for kinematic rupture modeling; Ye *et al.*, 2016]. For instance, scaling relationships that evaluate the width and length of a fault plane as a function of moment magnitude can be used to determine the geometry of an earthquake rupture for a given scenario. Moreover, randomness and heterogeneity of spatial earthquake slip distribution, which have major influence on tsunami hazard assessment [Geist, 2002; Løvholt *et al.*, 2012; Goda *et al.*, 2014, 2015; Davies *et al.*, 2015], can be characterized by wavenumber spectra [Mai and Beroza, 2002; Lavallée *et al.*, 2006]. Possible realizations of constrained random slip fields are normally generated using spectral synthesis methods and integrated into probabilistic tsunami hazard and risk assessment [Goda *et al.*, 2014, 2015; Fukutani *et al.*, 2015; Goda and Abilova, 2016]. It is noted that the above-mentioned advanced earthquake source modeling goes beyond the current practice of simpler methods, which typically define dimensions of the fault rupture deterministically using existing scaling relationships and assign a uniform slip over the fault rupture plane. The adoption of probabilistic tsunami hazard and risk methods has been popular after recent mega tsunamis.

The probabilistic tsunami hazard and risk assessment can be classified into two categories: one is stochastic earthquake source modeling [Goda *et al.*, 2014; Goda and Abilova, 2016] and another is a stochastic logic-tree approach [Horspool *et al.*, 2014; Fukutani *et al.*, 2015]. Both approaches require scaling relationships of fault parameters (e.g. width and length) for a given magnitude, however, the generalization of such scaling models is still poorly developed for tsunamigenic earthquakes.

To develop scaling relationships for spatial slip distribution parameters, Mai and Beroza [2002] analyzed 44 finite-fault rupture models that were obtained from source inversion studies, and modeled wavenumber spectra using von Kármán, Gaussian, and fractal models. They suggested that the von Kármán model is most suitable among the tested models for characterizing the heterogeneity of earthquake slip. The anisotropic von Kármán spectrum can be defined by three parameters; the Hurst number characterizes the spectral decay in the large wavenumber range, whereas the correlation lengths along dip and strike directions capture anisotropic spectral behavior and determine the spectral level in the small wavenumber range. Subsequently, prediction models of the von Kármán parameters were proposed by relating the values of the spectral parameters to moment magnitude M_w. The key findings of their study are: (i) the Hurst number, having relatively large variability, does not depend on earthquake magnitude, and (ii) the scaling of the correlation lengths is proportional to the scaling of the finite-fault dimensions. Recently, Goda *et al.* [2014] analyzed 11 source models for the M_w9 Tohoku earthquake (developed by different researchers). They found that although the magnitude ranges of the underlying data are different from the source models analyzed by Mai and Beroza [2002], the results for the Tohoku earthquake are broadly consistent with the Mai–Beroza scaling relationships; see also Goda and Abilova [2016].

Currently, there is a critical gap in stochastic earthquake source modeling: lack of comprehensive evaluations of the spatial slip distribution parameters for large mega-thrust subduction earthquakes which potentially trigger massive tsunamis. The events analyzed by Mai and Beroza [2002] were crustal earthquakes of magnitudes up to 8 and were not of tsunami type, whereas source models analyzed by Goda *et al.* [2014] were specifically for the 2011 Tohoku earthquake. Hence, a question as to whether existing scaling relationships can be used for very large subduction earthquakes remains unanswered due to the inherent limitation of the current models. This limitation is also applicable to geometry and slip statistics parameters. For instance, scaling relationships by Blaser *et al.* [2010] do not include recent mega-thrust subduction events (e.g. 2011 Tohoku earthquake), whereas scaling relationships by Murotani *et al.* [2013] are specific to Japanese subduction earthquakes. None of the existing relationships cover all necessary parameters for stochastic source modeling. Moreover, uncertainty and dependency of predicted source parameters are not fully characterized; in other words, existing relationships cannot be used as multivariate prediction models of the parameters. Hence, comprehensive updating of scaling relationships of key source parameters is highly desirable.

In this study, finite-fault rupture models that are compiled in the SRCMOD database (Mai and Thingbaijam, 2014) are analyzed to develop scaling relationships for various source parameters. Three types of source parameters are considered: (i) geometry parameters including the fault width W, fault length L, and fault area S; (ii) slip statistics parameters including the mean slip D_a, maximum slip D_m, and Box-Cox power λ; and (iii) spatial slip distribution parameters including the correlation lengths along dip and strike directions A_z and A_x and the Hurst number H. As of December 2015, SRCMOD contains 317 earthquake models, covering the earthquake magnitudes up to 9.2 (i.e. 2004 Indian Ocean event), and is the most comprehensive database for finite-fault rupture models in the public domain. This offers a unique opportunity to assess scaling relationships of the earthquake source parameters over a wide range of earthquake magnitudes and for different earthquake types (e.g. oceanic subduction events).

This study uniformly and systematically analyzes earthquake source models contained in the SRCMOD database and evaluates various source parameters to develop new scaling relationships for stochastic tsunami simulation. In analyzing inversion-based source models, effective dimensions of the finite-fault models are considered by following the procedures suggested by Mai and Beroza [2000] and Thingbaijam and Mai [2016] (see Sec. 3.1). The consideration of effective dimensions essentially allows focusing on the major characteristics of earthquake slip within the fault plane by ignoring sub-faults with near-zero or zero slip values along the edges of the fault plane. Note that these small slip values may not be robust features of the physical rupture process and their errors may be significant [Satake *et al.*, 2013; Ye *et al.*, 2016]. Using the entire SRCMOD database, preliminary analyses are first carried out to determine usable source models for the parameter estimation; this is performed by inspecting details of the model features (e.g. model complexity and spatial resolution) as well as the event information (e.g. deep events and small swarm events are excluded). The selection of the usable source models is discussed in Sec. 2. Based on the preliminary analyses, a set of 226 source models, out of 317 models, is selected and subsequently, the source parameters for these models are estimated for further investigations. The source models are categorized into "tsunamigenic" and "non-tsunamigenic" types (which broadly correspond to subduction and non-subduction types). The classification of the models aims at capturing different scaling features of tsunamigenic earthquakes, which usually have gentler dip angles and thus the rupture can be extended more toward the down-dip direction, in comparison with non-tsunamigenic earthquakes that occur in the upper continental crust with relatively steep dip angles. In Sec. 3, scaling relationships of the source parameters are developed and are compared with existing models in the literature. In Sec. 4, applications of the developed scaling relationships are demonstrated by synthesizing earthquake source models for simulating tsunamis in the Tohoku region of Japan (near the Sendai plain). The examples are to provide practical guidance as to how the developed scaling relationships can be implemented in stochastic tsunami simulation.

The effects of magnitude scaling of the source parameters and their uncertainties are investigated.

The novelty and significance of the current study are that new scaling relationships for a comprehensive set of earthquake source parameters (not only for geometry and slip parameters but also for spatial slip distribution parameters) are developed consistently based on the extensive SRCMOD database, which is critically lacking in the literature. The developed relationships can be implemented as multivariate probabilistic prediction models of the source parameters because both uncertainty and dependency of the model prediction residuals are evaluated statistically. The new models facilitate the synthesis of realistic earthquake rupture models and will enable various investigations using stochastic earthquake scenarios, including reliability analysis of coastal structures against massive tsunamis [e.g. Tsujio *et al.*, 2015] and probabilistic tsunami hazard and risk assessment [Fukutani *et al.*, 2015; Goda and Abilova, 2016].

2. Finite-Fault Rupture Models

2.1. *SRCMOD database*

SRCMOD is a comprehensive and growing on-line database of finite-fault rupture models [Mai and Thingbaijam, 2014]. It includes inversion-based rupture models that have been published in the literature, and is the largest public database of this kind, consisting of 317 rupture models from 155 earthquakes as of December 2015. The SRCMOD website (http://equake-rc.info/srcmod/) presents a collection of rupture models with enhanced visualization tools and supplementary information. The database is useful for analyzing the key features of the source parameters statistically and for developing scaling relationships of the source parameters [e.g. Mai and Beroza, 2000, 2002].

The rupture models that are included in the SRCMOD database are based on source inversion analyses of geophysical data observed during major seismic events in the past. The data type ranges from: teleseismic, strong motion, geodetic, tsunami, remote-sensing, and joint use of different types of data. The quality of the inversion models in terms of geophysical data and inversion methods is heterogeneous. The finite-fault source models, despite their own limitations [e.g. model resolution and robustness; Beresnev, 2003], attempt to produce plausible images of earthquake rupture processes by achieving the consistency between observed data and geophysical model predictions, and are considered to be objective and theoretical (note: assessing the credibility of the developed rupture models is beyond the scope of this study). It is important to note that the data (e.g. source dimensions) compiled in the SRCMOD database are different from those inferred based on the spatial distribution of aftershocks following a large mainshock, which are typically used as source dimension data in developing empirical scaling laws [e.g. Wells and Coppersmith, 1994; Blaser *et al.*, 2010].

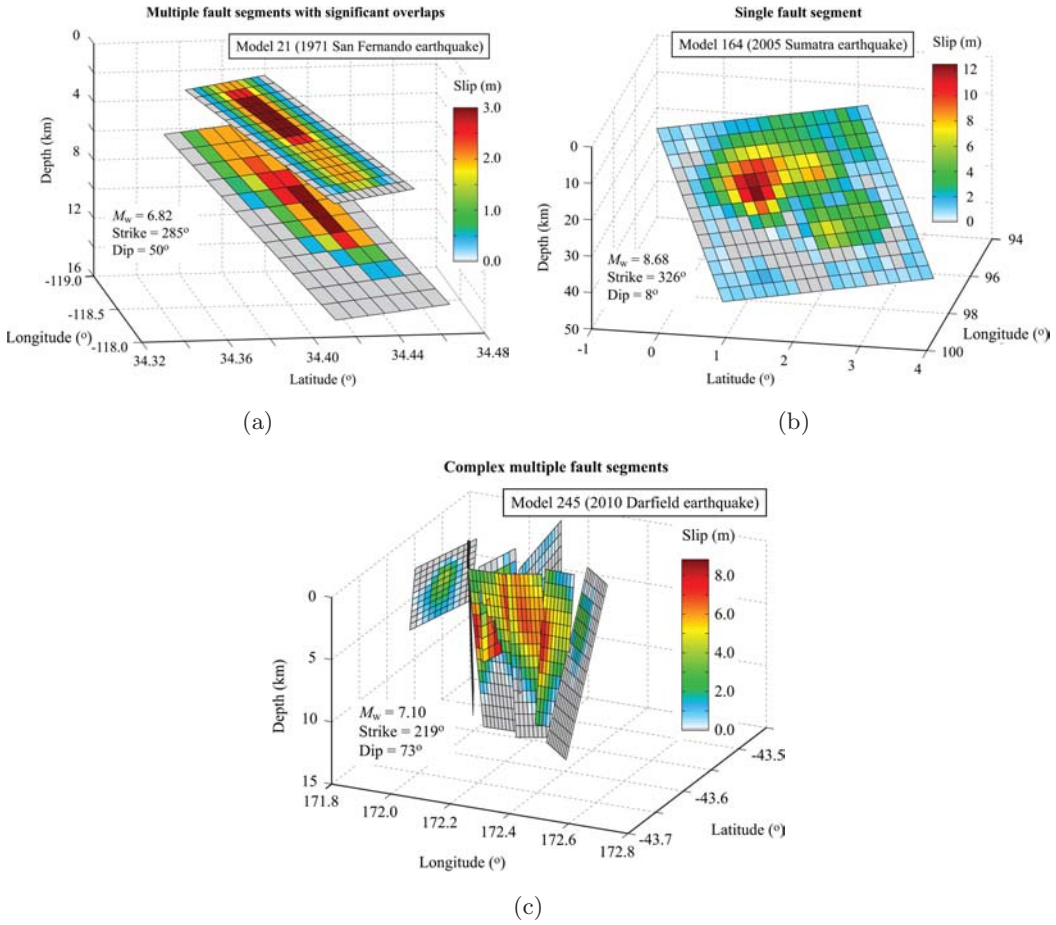

Fig. 1. Three examples of finite-fault rupture models.

Three rupture models are illustrated in Fig. 1. In general, a finite-fault rupture model is represented by a set of sub-faults, geometry of which can be characterized by either single segment (model 164; Fig. 1(b)) or multiple segments (models 21 and 245; Figs. 1(a) and 1(c)). The resolution of model discretization is influenced by available data and inversion methods. Each sub-fault has estimated earthquake slip (and other parameters, depending on the details of the inversion models), and thus the rupture models are useful for investigating the spatial features of the earthquake rupture process in addition to geometry parameters.

For developing empirical scaling relationships of earthquake source parameters for stochastic tsunami simulation, the following source parameters are extracted/estimated from the finite-fault rupture models in the SRCMOD database: the fault width W, fault length L, fault area S, mean slip D_a, maximum slip D_m, Box-Cox power λ, correlation length along dip A_z, correlation length along strike A_x, and Hurst number H. In this study, the spatial extent of earthquake rupture is evaluated as "effective dimensions" of the source model [Mai and Beroza, 2000;

Thingbaijam and Mai, 2016; Ye *et al.*, 2016; see Sec. 3.1]. This essentially reduces the dimensions of some of the original source models by focusing on the major slip features. It is noteworthy that the consideration of the effective source dimensions affects not only fault geometry parameters but also other parameters, such as mean slip, because they are estimated based on "effective" source models. It is arguable as to which of the dimensions, i.e. effective versus original, is suitable for earthquake source modeling. The fundamental difficulties of this problem are that the boundaries of the rupture models are defined only loosely (sometimes they are determined subjectively by the developers of the models) and that the estimated slip values, especially small slips (e.g. gray color patches of the source models shown in Fig. 1), may be associated with significant uncertainty (i.e. some of the estimated slip values may not be the stable feature of the model). Unfortunately, it is rare that the developers of the rupture models indicate such uncertainties explicitly.

2.2. *Model selection*

A model selection is carried out by taking into account various selection criteria, such as earthquake characteristics, model resolution, and model complexity. First, all source models are individually inspected to determine the applicability of the rupture model for spectral analysis. The spectral analysis requires a slip distribution that can be mapped onto a single fault plane (e.g. model 164 in Fig. 1(b)). The rupture models consisting of multiple segments with good alignment may be usable and can be adopted for further investigations. Among the 317 source models, some models consist of multiple segments that have major overlaps with large slips (e.g. model 21 in Fig. 1(a)) or have complex configurations of multiple segments (e.g. model 245 in Fig. 1(c)). Such complex models are excluded from the analysis. Moreover, the following model selection criteria are considered: (i) earthquake magnitude is greater than 5.5, (ii) deep inslab events are excluded, (iii) the number of non-zero slip subfaults is greater than 40, (iv) the number of sub-faults along dip/strike direction is equal to or greater than 4, and (v) for a given earthquake, only one model (typically latest one) from the same developers is accepted. The first criterion essentially eliminates the source models related to swarm events. The second criterion excludes deep inslab events (e.g. 2009 Padang earthquake). The third and fourth criteria are considered to exclude rupture models with low spatial resolutions in terms of slip distribution to have robust estimates of the spatial slip distribution parameters; they are interpreted as loose constraint and acceptance/rejection of the models was decided based on the stability of the spectral analysis results. The implementation of the preceding model selection criteria results in a set of 226 rupture models.

This dataset is further divided into 100 tsunamigenic models and 126 non-tsunamigenic models. The determination of "tsunamigenic" versus "non-tsunamigenic" is based on the detailed information of individual events. Tsunamigenic events typically occur at the interface between the subducting oceanic plate

and the overriding continental plate, and the dominant faulting mechanism for the tsunamigenic models is reverse faulting. It is noted that strike-slip events occurring at the oceanic ridge boundary (e.g. 2003 Carlsberg Ridge event) are included in the non-tsunamigenic subset, while outer-rise normal faulting events (e.g. 2007 Kuril Islands event) are included in the tsunamigenic subset.

Figure 2(a) shows the spatial distribution of the selected 226 source models, distinguishing tsunamigenic and non-tsunamigenic models. The tsunamigenic models

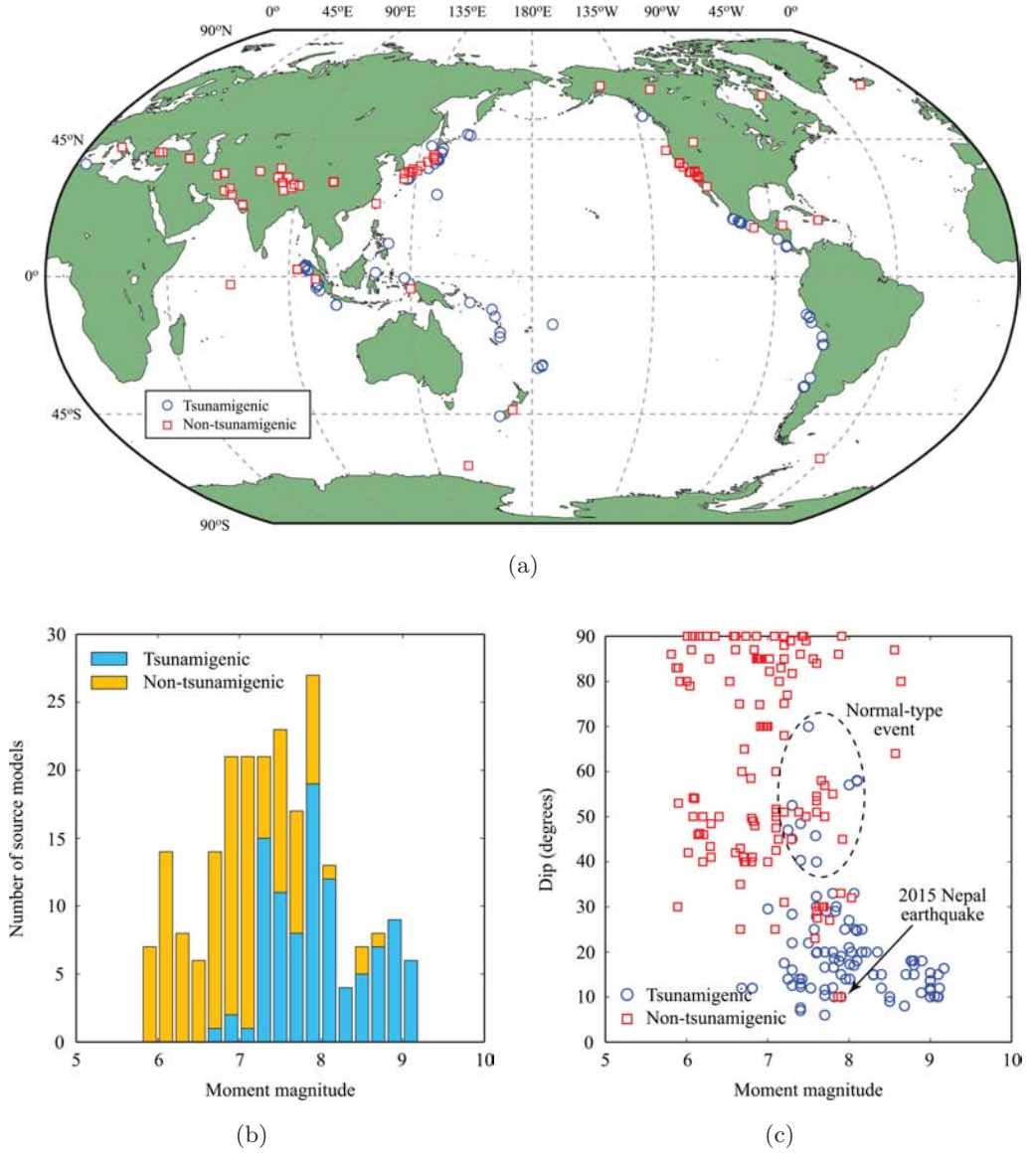

Fig. 2. Characteristics of 226 source models: (a) locations, (b) histogram in terms of moment magnitude, and (c) moment magnitude–dip angle relationship.

are located in ocean areas, whereas the majority of the non-tsunamigenic models are on land areas. Figure 2(b) presents a histogram of the 226 source models in terms of moment magnitude. It is clear that the earthquake magnitudes for the tsunamigenic models are greater than those for the non-tsunamigenic models. Typically, the moment magnitude of the tsunamigenic models ranges from 7.0 to 9.2, whereas that of the non-tsunamigenic models is distributed between 5.8 and 8.0. Figure 2(c) shows the magnitude–dip angle relationship, indicating that the classification of tsunamigenic versus non-tsunamigenic types essentially separates the models in terms of dip angle. The tsunamigenic models have gentler dip angles (typically less than 40°, except for the outer-rise normal faulting events). In Fig. 2(c), two non-tsunamigenic data points that have magnitudes of about 8 and dip angles of about 10° are for the 2015 Nepal earthquake, which is in fact a low-angle reverse faulting event occurring in the continental subducting plate.

3. Source Parameter Estimation and Development of Scaling Relationships

3.1. *Analysis methods*

The source parameters (i.e. geometry, slip statistics, and spatial slip distribution) are estimated through effective dimension analysis [Mai and Beroza, 2000], Box-Cox analysis, and Fourier spectral analysis [Mai and Beroza, 2002; Goda *et al.*, 2014]. Figure 3 shows the analysis procedures for the source parameter estimation. The salient features of the methods are presented in the following; interested readers should consult with the above-mentioned papers and references cited therein for more detailed explanations.

First, sub-faults having zero slips along the edges of the rupture plane are removed from the original source models as they are considered as unimportant features of the rupture model. To focus on the major slip features of the original source models, effective source dimensions are evaluated from the autocorrelation dimensions W_{AC} and L_{AC} along dip or strike. W_{AC} and L_{AC} are calculated as the area under the autocorrelation function of one-dimensional slip function normalized by the zero lag value [Mai and Beroza, 2000]:

$$W_{AC} = \frac{\int_{-\infty}^{\infty} (f_W * f_W) ds}{f_W * f_W|_{s=0}} \quad \text{and} \quad L_{AC} = \frac{\int_{-\infty}^{\infty} (f_L * f_L) ds}{f_L * f_L|_{s=0}}, \tag{1}$$

where f_W or f_L is the one-dimensional slip function along dip or strike (which can be computed from the original slip distribution by summing up the slip values along strike or dip), and $f_W{*}f_W$ or $f_L{*}f_L$ represents the auto-correlation function of the one-dimensional slip. The estimation of the final effective source dimensions is iterative. The largest dimension that fits the auto-correlation width/length (as in Eq. (1)) is determined such that the difference between the two is less than or equal to the sub-fault size. The trimming process is done by removing any row/column

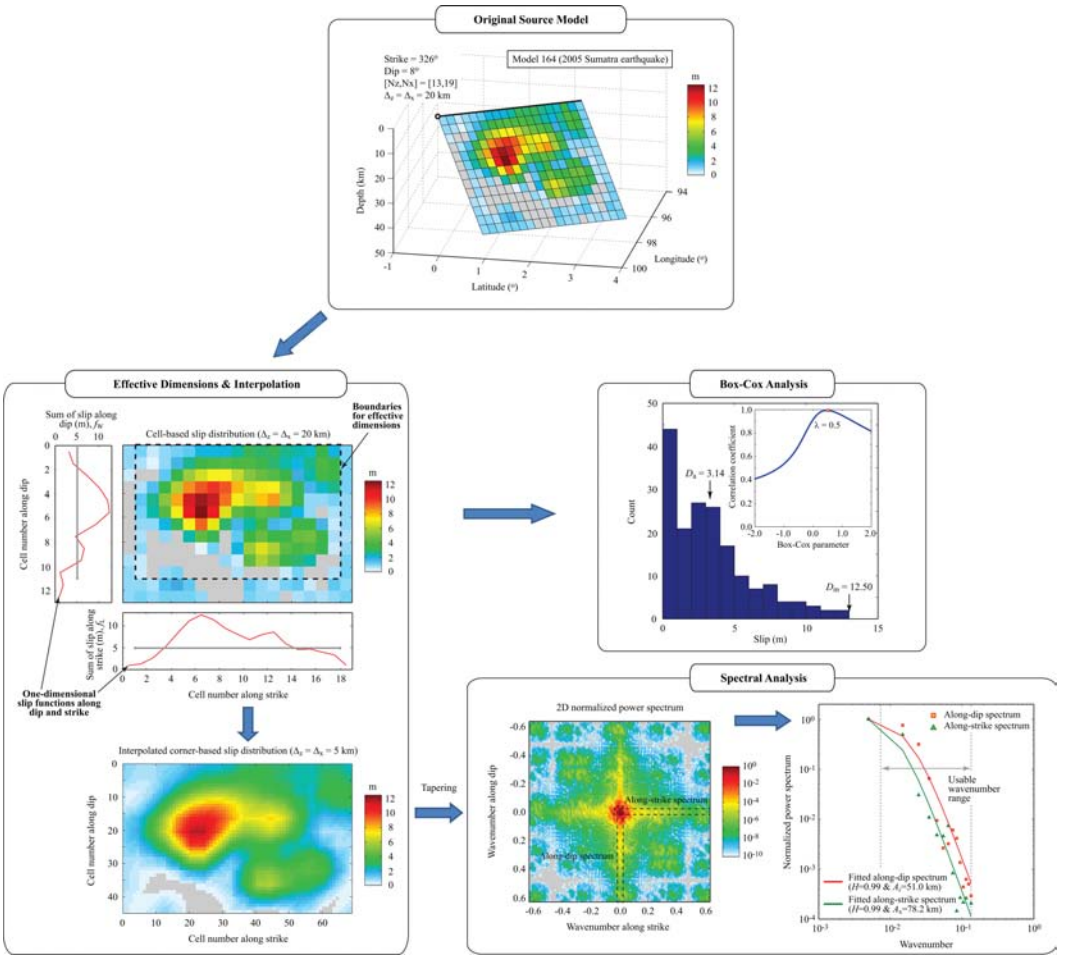

Fig. 3. Procedures for source parameter estimation.

at the fault edge from the slip distribution if maximum slip in this row/column is less than or equal to a threshold value of 0.01. Note that when the top-edge of the rupture plane is located at the Earth surface, and a large-slip asperity is encountered within 5 km depth, the top-edge of the fault plane is not trimmed. See Thingbaijam and Mai [2016] for further details. Depending on the slip distribution of the source model, estimated effective dimensions can be smaller than the original source dimensions. Using the effective source models, mean slip and maximum slip, D_a and D_m, are evaluated.

An illustration of effective dimension analysis of an earthquake source model is shown in Fig. 3 (top figure in *Effective Dimensions & Interpolation* panel). Using the original source model, the slip functions along dip and strike directions can be evaluated and are shown in the side panels to the left-hand side and bottom of the slip distribution; gray lines shown in the side panels are the effective dimensions that

are estimated through the iterative row/column removing procedures. For the slip distribution shown in Fig. 3, two rows are removed from the bottom (i.e. down-dip edge), whereas one column each is removed from both right-hand and left-hand sides of the fault plane (i.e. strike edges). The dotted rectangular represents the effective source dimension for the slip distribution.

The effective dimensions of the 226 source models that are used to develop scaling relationships are evaluated. Figure 4 compares the width, length, and mean slip based on effective and original source models. The results shown in Figs. 4(a)

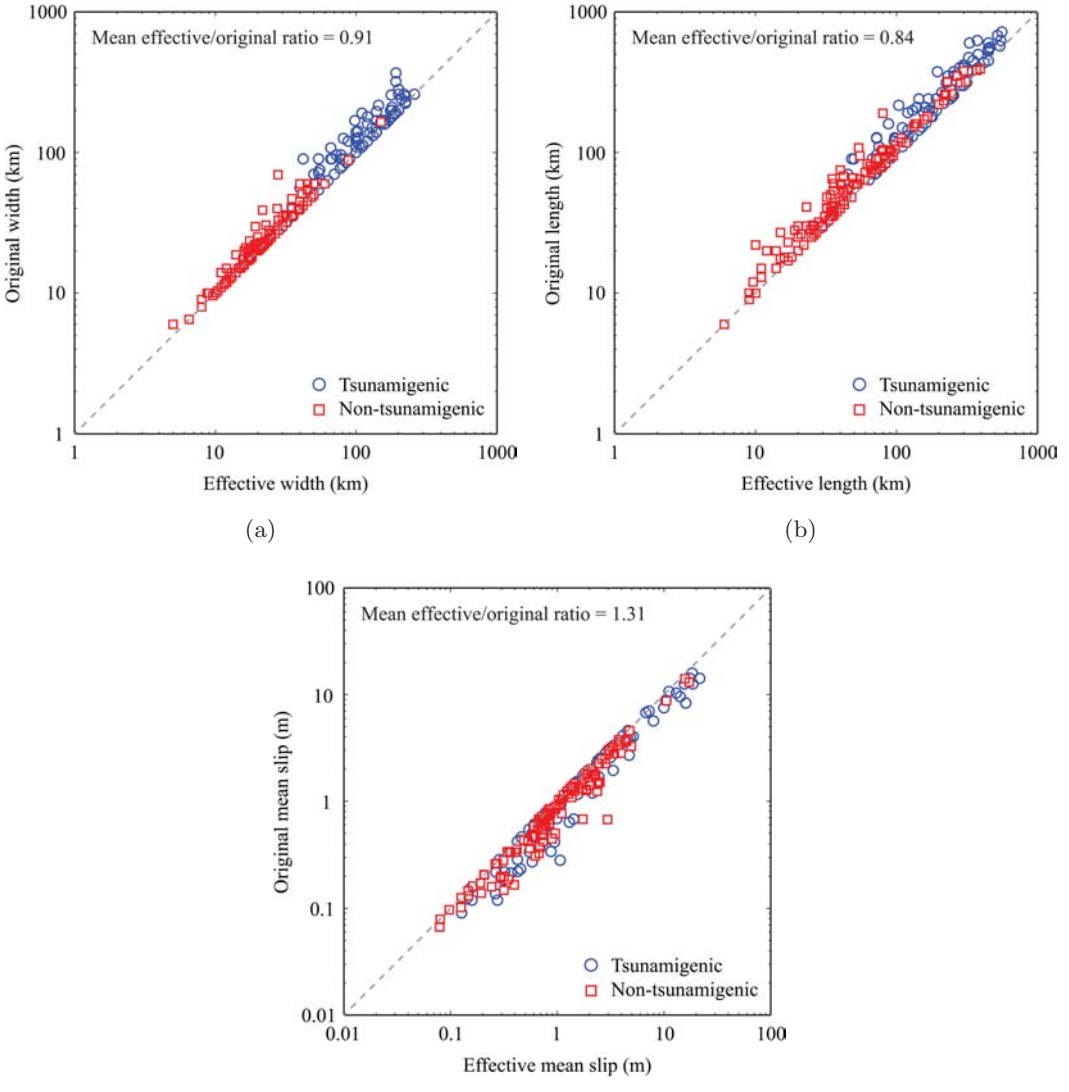

Fig. 4. Comparison of source parameters based on effective and original source models: (a) fault width, (b) fault length, and (c) mean slip.

and 4(b) indicate that overall, effective dimensions are smaller than original dimensions (note: for some models the effective and original dimensions are identical). The average ratios of the effective dimensions to original dimensions are 0.91 and 0.84 for the width and length, respectively. Figure 4(c) shows that the mean slip values for the effective source models are greater than those for the original source models because the effective dimensions essentially remove the minor slip values along the edges of the fault plane. The mean ratio of the effective mean slip to original mean slip is about 1.31.

Subsequently, the Box-Cox analysis of a slip distribution is carried out to characterize the probability distribution of slip values within the fault plane. It identifies the best power parameter such that a non-normal random variable (original data) can be transformed to a normal random variable. It is noted that the majority of inverted source models have slip values that are distributed with heavier right tails with respect to the normal distribution (i.e. positive skewness). The motivation of this approach is that in generating random fields using the Fourier integral method [Pardo-Iguzquiza and Chica-Olmo, 1993], the output slip distribution is normally distributed. To achieve the non-normal distribution, inverse Box-Cox transformation may be applied [Goda *et al.*, 2014]. The Box-Cox transformation is defined as:

$$Y = \frac{X^{\lambda} - 1}{\lambda} \quad (\lambda \neq 0), \tag{2}$$

where X is the original variable (i.e. non-normal) and Y is the transformed variable (i.e. normal), and λ is the power parameter. When $\lambda = 0$, the Box-Cox transformation corresponds to the lognormal transformation. The best power parameter can be identified by calculating the linear correlation coefficient of the standard normal variable and the transformed variable of the slip values (after standardization) for a range of λ values (typically -2 to 2). The value of λ that achieves the maximum linear correlation coefficient can be adopted. For the illustrative case shown in Fig. 3, a histogram of the slip values of the effective source model is shown in *Box-Cox Analysis* panel, exhibiting the positive skewness. For the slip data, $\lambda = 0.5$ is obtained as the best power parameter.

The spectral analysis of a slip distribution is carried out based on the procedures given by Mai and Beroza [2002] and Goda *et al.* [2014]. In this study, the von Kármán wavenumber spectrum $P(k)$ is considered for characterizing the spatial slip distribution [Mai and Beroza, 2002]:

$$P(k) \propto \frac{A_z A_x}{(1 + k^2)^{H+1}}, \tag{3}$$

where k is the wavenumber, $k = (A_z^2 k_z^2 + A_x^2 k_x^2)^{0.5}$ (note: wavenumber is proportional to the reciprocal of wavelength), A_z and A_x are the correlation lengths along dip and strike directions, respectively, and H is the Hurst number. The correlation lengths

determine the absolute level of the power spectrum in the low wavenumber range, and capture the anisotropic spectral features of the slip distribution (when different correlation lengths are specified for dip and strike directions). The Hurst number controls the slope of the power spectral decay in the high wavenumber range, and is theoretically constrained to range between 0 and 1. The analysis method consists of several steps as follows.

(1) Typically, slip values of the original source model are specified at individual sub-faults (i.e. cell-based slip distribution). To transform the cell-based slip distribution into a corner-based slip distribution, a quarter of the slip value for each of the sub-faults is assigned at the four corners and then the sum of the assigned slip values at the corner grids of the slip distribution is calculated. Subsequently, the corner-based slip distribution is interpolated with a smaller grid size. The grid size for interpolation is not smaller than one-fifth of the original grid resolution. This is illustrated in the bottom figure in *Effective Dimensions & Interpolation* panel of Fig. 3. Then, the slip distribution is tapered using a Hanning window by adding two rows/columns to all sides of the source model.
(2) The two-dimensional Fast Fourier Transform (FFT) of the interpolated and tapered slip distribution is computed, and the amplitude spectrum is normalized with respect to the maximum value (left figure in *Spectral Analysis* panel of Fig. 3). The grid number of the two-dimensional FFT is the nearest higher power of 2 based on the larger source dimension of the fault plane.
(3) The circular average of the normalized wavenumber spectrum is calculated [Anguiano *et al.*, 1993] and the fractal dimension D is determined based on the least squares fitting. The obtained fractal dimension is then converted to the Hurst number: $H = 3 - D$. In this study, the estimated value of D is constrained to lie between 2 and 3 (because H is theoretically constrained to range between 0 and 1); accordingly, the minimum and maximum values of H are set to 0.01 and 0.99, respectively (as practical limiting values), noting that $H = 1$ corresponds to so-called "k-squared" model [Mai and Beroza, 2002; see Eq. (3)]. For the identified value of H, one-dimensional search of suitable correlation lengths for dip and strike directions is carried out by minimizing the norm between the along-dip/along-strike wavenumber spectrum and the analytical von Kármán model (with varying correlation lengths). The spectral fitting for the dip and strike directions is illustrated in the right figure in *Spectral Analysis* panel of Fig. 3. For this example, the Hurst number is estimated to be 0.99, whereas the correlation lengths along dip and strike directions are 51 km and 78.2 km, respectively.

Several remarks regarding the above-mentioned spectral analysis are necessary. In step (1), interpolation and tapering of the slip distribution prior to the two-dimensional FFT affect the estimation of the Hurst number and the correlation lengths. The interpolation essentially introduces additional spectral components in the large wavenumber range. On the other hand, tapering may alter the spectral

components of the slip distribution when it has large slip concentrations near the edges of the fault plane [e.g. source models for the 2011 Tohoku earthquake; Goda *et al.*, 2014]. In such cases, tapering forces the slip distribution to decay to zero over two grid-size distances (as determined by the Hanning window). This may lead to underestimation or overestimation of the spectral decay feature due to wavenumber spectral content that is artificially introduced by tapering, more significantly in the large wavenumber range. On the other hand, large slip concentrations along the edges of the fault plane and abrupt termination of the slip distribution (when tapering is not considered) may also be regarded as unrealistic, although tapering of the slip along the top-edge may adversely introduce biases in the estimated spatial slip distribution parameters when large asperities along the top-edge are real features of the earthquake rupture. In this study, by default, interpolation and tapering are considered. In Sec. 3.2.3, the effects of interpolation and tapering are examined by conducting several additional analyses with/without interpolation/tapering.

3.2. *Development of scaling relationships of the earthquake source parameters*

Using the analysis results for the 226 models in the SRCMOD database, scaling characteristics of fault geometry parameters (i.e. L, W, and S), slip statistics parameters (D_a, D_m, and λ), and spatial slip distribution parameters (A_z, A_x, and H) are investigated. The results of the investigations are presented in Figs. 5–12, and will be discussed in Secs. 3.2.1–3.2.3.

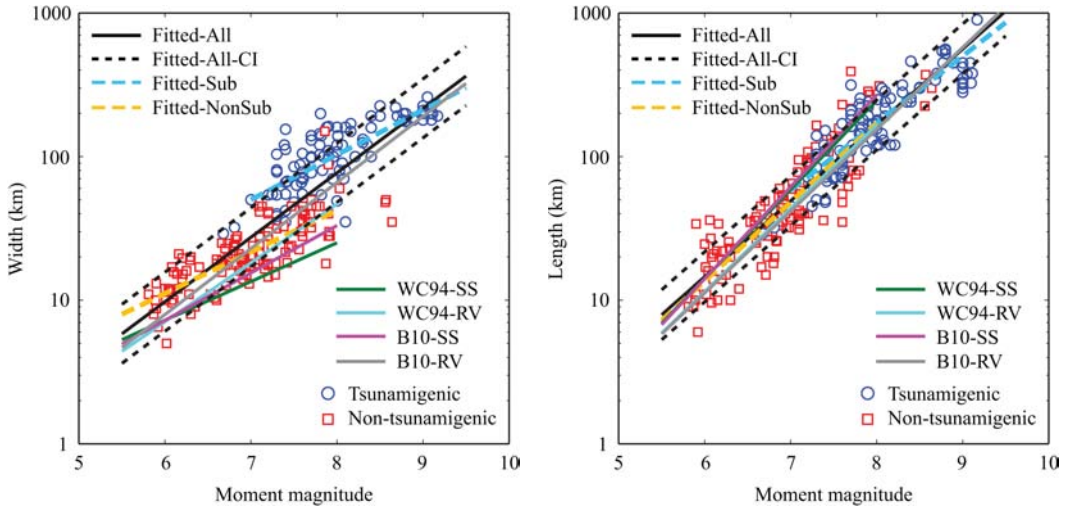

(a) (b)

Fig. 5. (a) Moment magnitude–fault width relationship and (b) moment magnitude–fault length relationship in comparison with existing relationships by Wells and Coppersmith [1994] [WC94] and Blaser *et al.* [2010] [B10].

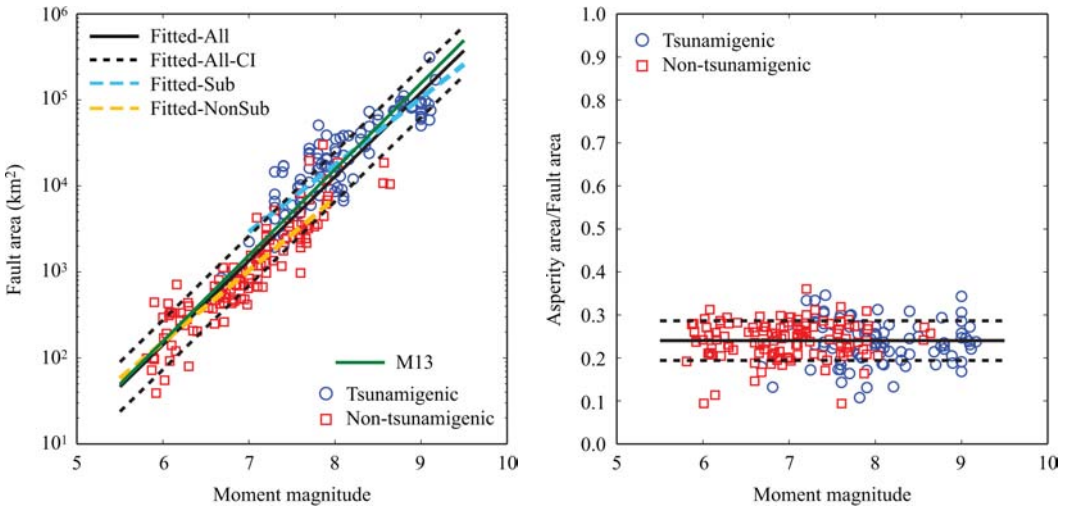

(a) (b)

Fig. 6. (a) Moment magnitude–fault area relationship in comparison with an existing relationship by Murotani *et al.* [2013] [M13] and (b) moment magnitude–asperity area-to-fault area ratio relationship.

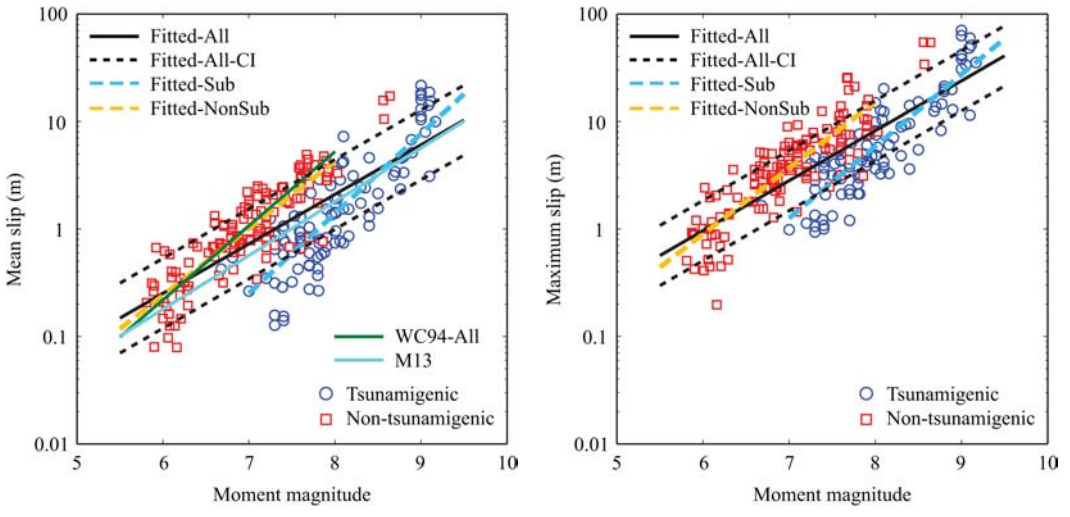

(a) (b)

Fig. 7. (a) Moment magnitude–mean slip relationship and (b) moment magnitude–maximum slip relationship in comparison with existing relationships by Wells and Coppersmith [1994] [WC94] and Murotani *et al.* [2013] [M13].

For each of the source parameters, dependency of the parameters on M_w is examined. When a clear dependency on M_w is observed, regression analysis is carried out to develop scaling relationships by considering two cases: one case combines all model types while the other case distinguishes tsunamigenic models and non-tsunamigenic

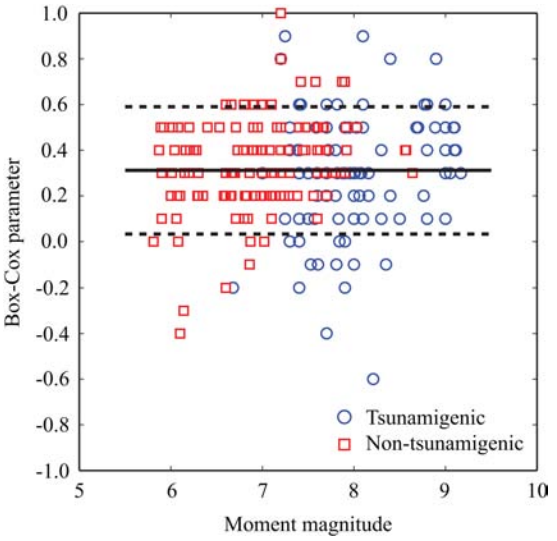

Fig. 8. Moment magnitude–Box-Cox parameter relationship.

models. The functional forms of the scaling relationships that are adopted in this study are:

$$\log_{10}\theta = a + bM_w + \sigma\varepsilon \tag{4}$$

and

$$\log_{10}\theta = I_T(a_T + b_T M_w) + I_{NT}(a_{NT} + b_{NT} M_w) + \sigma\varepsilon, \tag{5}$$

where θ is the source parameter of interest (e.g. L and W); a and b are the regression parameters (a_T, b_T, a_{NT}, and b_{NT} are also regression parameters for different subsets of the models; subscripts T and NT represent "tsunamigenic" and "non-tsunamigenic", respectively); σ is the standard deviation of regression residuals; ε is the standard normal variable (i.e. zero mean and unit standard deviation) and represents the randomness of the developed equation; I_T and I_{NT} are the indicator variables and take a value of 1 when the model is classified as tsunamigenic and non-tsunamigenic, respectively (otherwise zero). To facilitate the accessibility of the main results of this section, developed scaling relationships for the two cases are listed in Tables 1 and 2. It is highlighted that the developed scaling relationships are essentially probabilistic prediction models because the epsilon term in Eqs. (4) and (5) captures the randomness of the scaling relationship. Furthermore, epsilon terms for different source parameters (e.g. ε_W and ε_{Az}) are correlated. As it is desirable to take into account such correlation in implementing the developed scaling relationships, the linear correlation coefficients of the epsilon terms are evaluated for the two cases, and the results are presented in Tables 3 and 4. When the correlation of the regression residuals is taken into account, a set of scaling relationships can

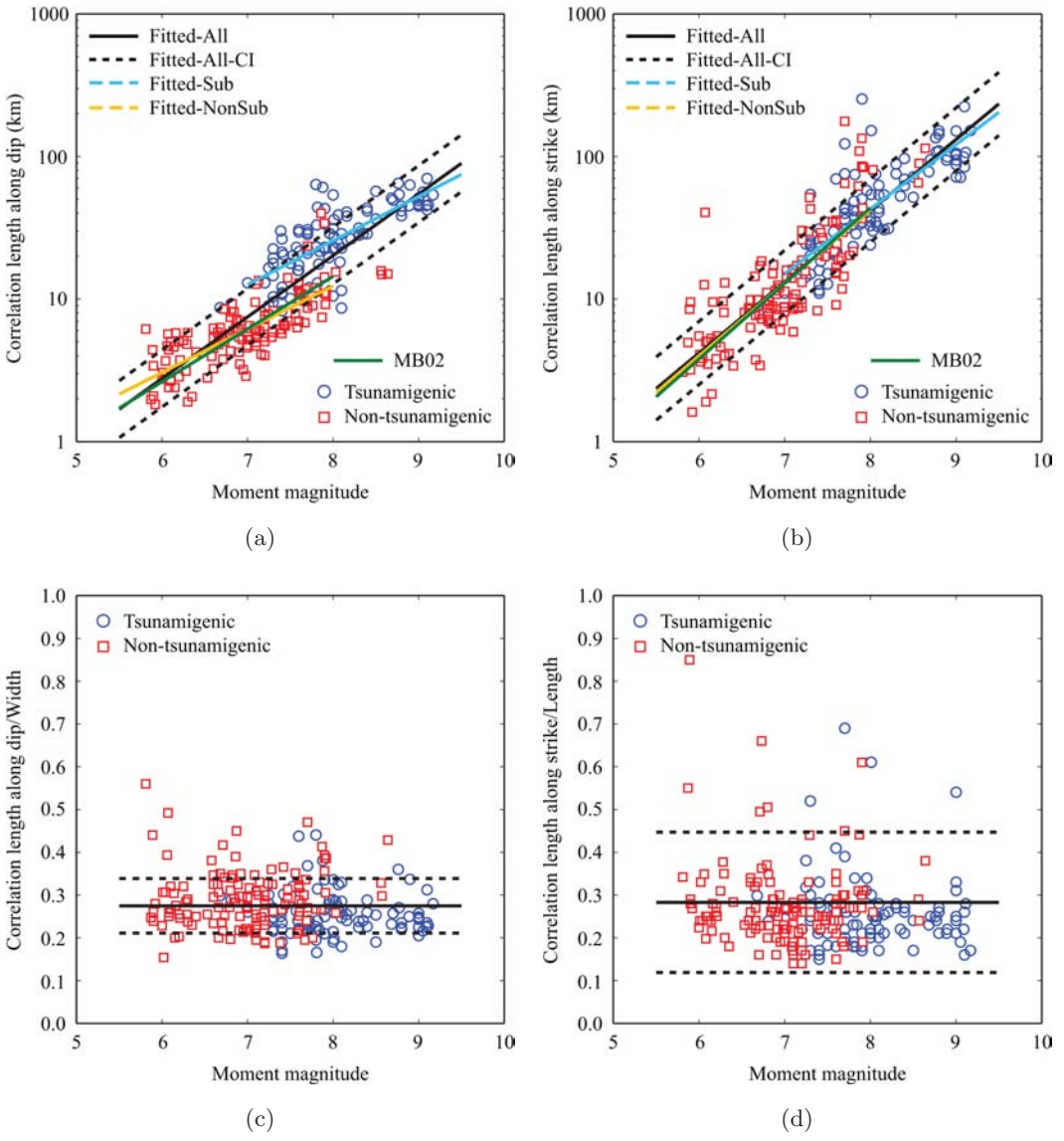

Fig. 9. (a) Moment magnitude–along-dip correlation length relationship and (b) moment magnitude–along-strike correlation length relationship in comparison with an existing relationship by Mai and Beroza [2002] [MB02], (c) moment magnitude–along-dip correlation length-to-fault width ratio relationship, and (d) moment magnitude–along-strike correlation length-to-fault length ratio relationship.

be implemented as multivariate prediction models of the source parameters. Such an application of the scaling relationships is demonstrated in Sec. 4. On the other hand, for λ and H, no clear dependency on M_w is observed (see Secs. 3.2.2 and 3.2.3), and therefore these parameters are modeled as independent random variables. The probabilistic information of λ and H is summarized in Table 5.

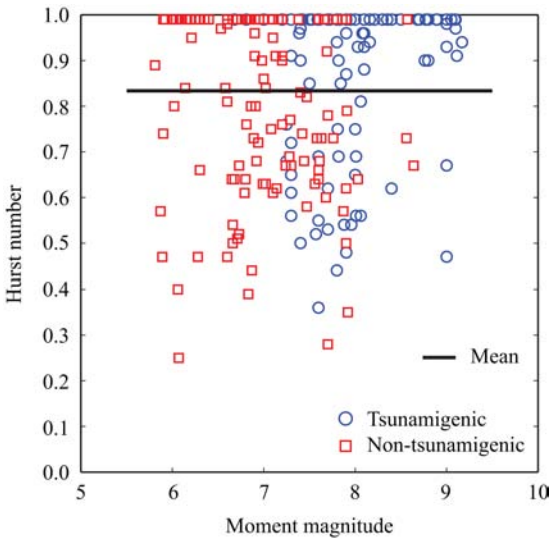

Fig. 10. Moment magnitude–Hurst number relationship.

3.2.1. *Scaling relationships for fault geometry parameters*

Figure 5 shows the fault width and length as a function of M_w by distinguishing tsunamigenic and non-tsunamigenic models. It can be observed that the M_w–W scaling behavior for the tsunamigenic models differs from that for the non-tsunamigenic models, whereas the M_w–L scaling behavior for the tsunamigenic models is similar to that for the non-tsunamigenic models. More specifically, for the same M_w values, W for the tsunamigenic models is greater than W for the non-tsunamigenic models. This is because the fault planes of the tsunamigenic models are dipping more gently than those of the non-tsunamigenic models (Fig. 2(c)) and thus the fault plane can be extended along down-dip direction, noting that the down-dip limit of the seismogenic zone is mainly controlled by the thermal condition of the subduction zone [Hyndman and Wang, 1995]. The results indicate that the distinction between tsunamigenic and non-tsunamigenic models is important for the fault width.

The fitted relationships for W and L indicate that the distinction of model types significantly improves the fitting performance of the developed scaling relationships for W because the standard deviation is decreased from 0.2053 to 0.1464 (Tables 1 and 2). On the other hand, no dramatic changes are observed for L. It is noteworthy that ε_W and ε_L are only weakly correlated; the calculated linear correlation is typically less than 0.15 (Tables 3 and 4). In Fig. 5, existing scaling relationships by Wells and Coppersmith [1994] [WC94] and Blaser *et al.* [2010] [B10] are also included. These existing models consider the distinction based on faulting mechanism; two faulting types, i.e. strike-slip (SS) and reverse (RV), are considered. The relationships by Wells and Coppersmith [1994] and the strike-slip relationships by Blaser *et al.* [2010] are mainly applicable to magnitudes up to 8, whereas the reverse

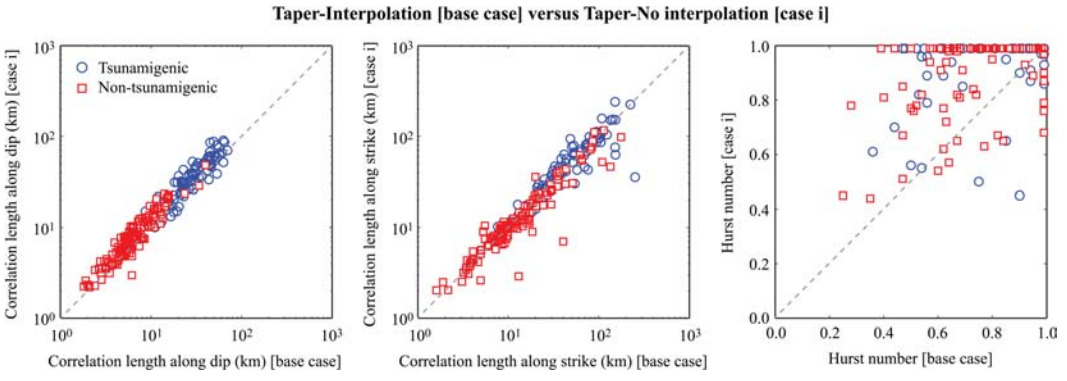

(a)

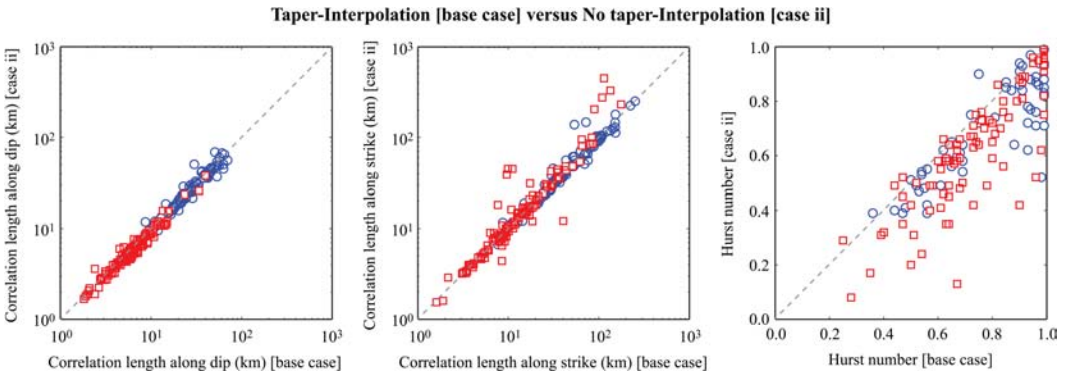

(b)

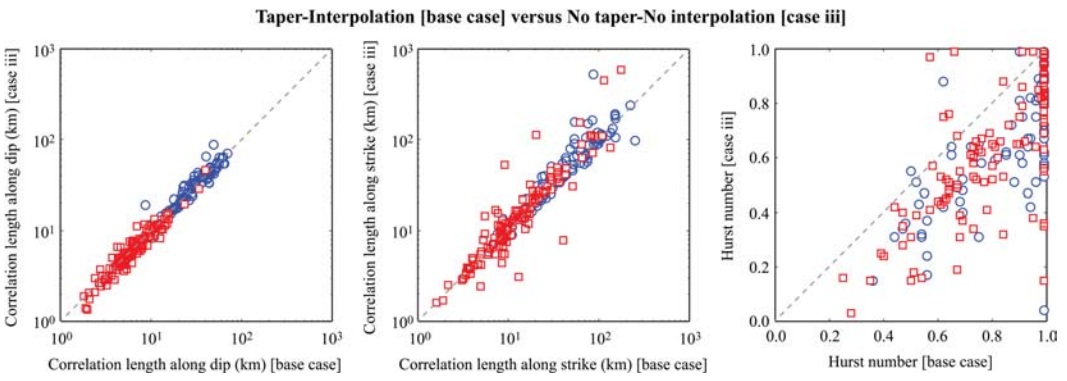

(c)

Fig. 11. Comparison of correlation lengths and Hurst number between the base case (with taper and with interpolation) and alternative cases: (a) with taper and without interpolation, (b) without taper and with interpolation, and (c) without taper and without interpolation.

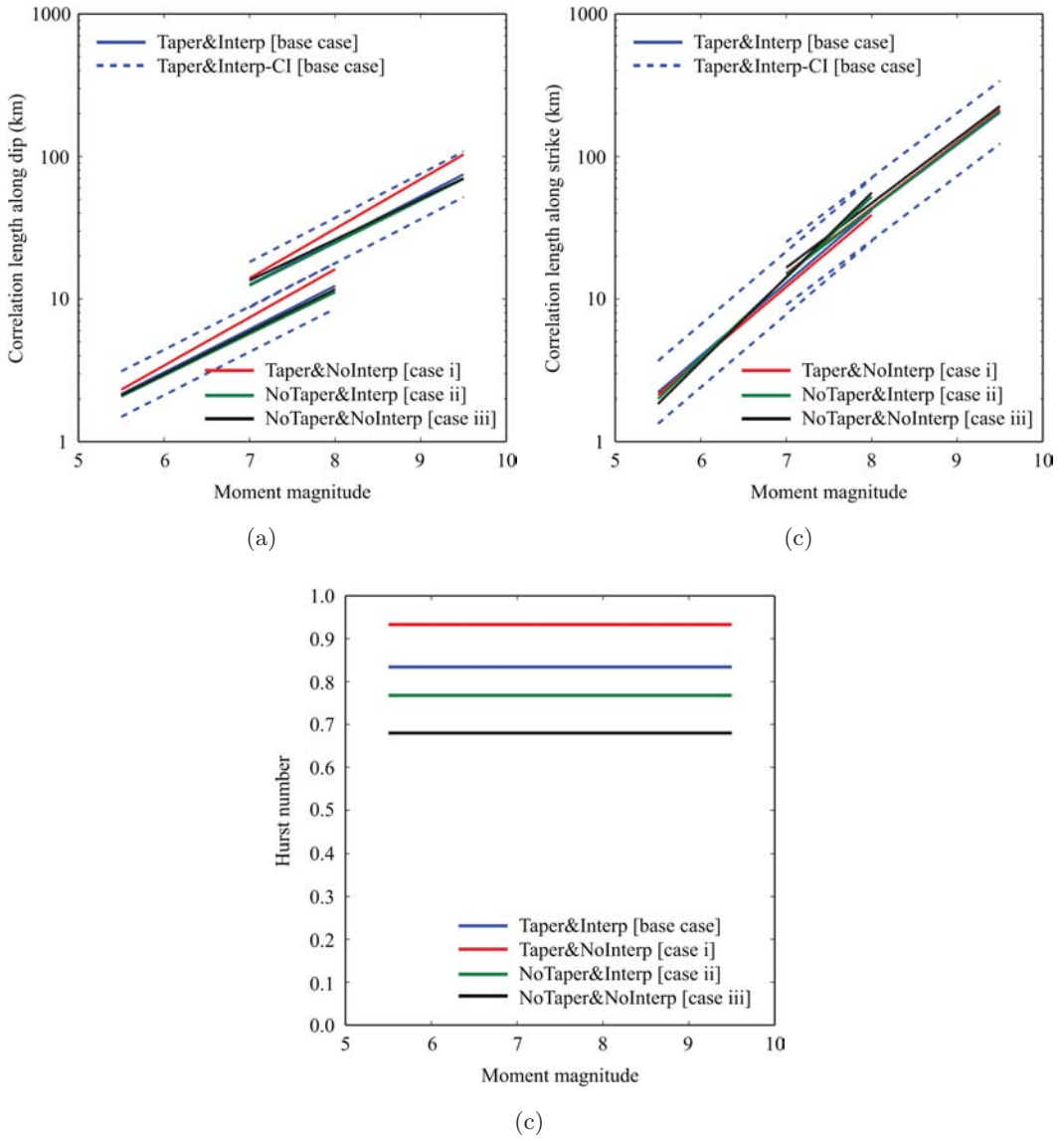

Fig. 12. Comparison of fitted relationships for spatial slip distribution parameters by considering the cases with/without taper and with/without interpolation: (a) correlation length along dip, (b) correlation length along strike, and (c) Hurst number.

relationships by Blaser *et al.* [2010] can be applied to events with magnitudes up to 9 (note: the Blaser *et al.* model is based on a number of large subduction events). The comparison of the scaling relationships for W indicates that the B10-RV relationship is similar to the prediction model for all earthquake types, whereas the WC94-RV relationship is consistent with the non-tsunamigenic data and is similar to the non-tsunamigenic model (Table 2). Note that the WC94-SS and B10-SS relationships are

Table 1. Scaling relationships of the width W, length L, fault area S, mean slip D_a, maximum slip D_m, correlation length along dip A_z, and correlation length along strike A_x without distinguishing model types.

Equations
$\log_{10} W = -1.7030 + 0.4488M_w + 0.2053\varepsilon_W$
$\log_{10} L = -2.0106 + 0.5289M_w + 0.1741\varepsilon_L$
$\log_{10} S = -3.7135 + 0.9777M_w + 0.2881\varepsilon_S$
$\log_{10} D_a = -3.3625 + 0.4606M_w + 0.3250\varepsilon_{Da}$
$\log_{10} D_m = -2.8031 + 0.4646M_w + 0.2790\varepsilon_{Dm}$
$\log_{10} A_z = -2.1448 + 0.4313M_w + 0.1996\varepsilon_{Az}$
$\log_{10} A_x = -2.3745 + 0.4994M_w + 0.2215\varepsilon_{Ax}$

Table 2. Scaling relationships of the width W, length L, fault area S, mean slip D_a, maximum slip D_m, correlation length along dip A_z, and correlation length along strike A_x by distinguishing tsunamigenic and non-tsunamigenic model types.

Equations
$\log_{10} W = I_T(-0.4877 + 0.3125M_w) + I_{NT}(-0.6892 + 0.2893M_w) + 0.1464\varepsilon_W$
$\log_{10} L = I_T(-1.5021 + 0.4669M_w) + I_{NT}(-2.1621 + 0.5493M_w) + 0.1717\varepsilon_L$
$\log_{10} S = I_T(-1.9898 + 0.7794M_w) + I_{NT}(-2.8512 + 0.8386M_w) + 0.2407\varepsilon_S$
$\log_{10} D_a = I_T(-5.7933 + 0.7420M_w) + I_{NT}(-4.3611 + 0.6238M_w) + 0.2502\varepsilon_{Da}$
$\log_{10} D_m = I_T(-4.5761 + 0.6681M_w) + I_{NT}(-3.7393 + 0.6151M_w) + 0.2249\varepsilon_{Dm}$
$\log_{10} A_z = I_T(-1.0644 + 0.3093M_w) + I_{NT}(-1.3350 + 0.3033M_w) + 0.1592\varepsilon_{Az}$
$\log_{10} A_x = I_T(-1.9844 + 0.4520M_w) + I_{NT}(-2.4664 + 0.5113M_w) + 0.2204\varepsilon_{Ax}$

Table 3. Linear correlation coefficients of regression residuals of the seven source parameters without distinguishing model types (corresponding to Table 1).

Variable	ε_W	ε_L	ε_S	ε_{Da}	ε_{Dm}	ε_{Az}	ε_{Ax}
ε_W	1.0	0.148	0.802	−0.809	−0.725	0.893	0.062
ε_L	0.148	1.0	0.709	−0.517	−0.464	0.242	0.736
ε_S	0.802	0.709	1.0	−0.889	−0.797	0.782	0.489
ε_{Da}	−0.809	−0.517	−0.889	1.0	0.895	−0.758	−0.330
ε_{Dm}	−0.725	−0.464	−0.797	0.895	1.0	−0.718	−0.308
ε_{Az}	0.893	0.242	0.782	−0.758	−0.718	1.0	0.261
ε_{Ax}	0.062	0.736	0.489	−0.330	−0.308	0.261	1.0

similar. These results suggest that the non-tsunamigenic relationships for W developed in this study are broadly consistent with the existing models that are available in the literature but the tsunamigenic relationships differ significantly from the existing ones. The differences may be attributed to the lack of mega-thrust subduction data in the previous studies. On the other hand, existing relationships for L are consistent with the data and the developed scaling models in this study.

Table 4. Linear correlation coefficients of regression residuals of the seven source parameters by distinguishing tsunamigenic and non-tsunamigenic model types (corresponding to Table 2).

Variable	ε_W	ε_L	ε_S	ε_{Da}	ε_{Dm}	ε_{Az}	ε_{Ax}
ε_W	1.0	0.139	0.708	−0.680	−0.545	0.826	0.035
ε_L	0.139	1.0	0.798	−0.595	−0.516	0.249	0.734
ε_S	0.708	0.798	1.0	−0.838	−0.699	0.680	0.545
ε_{Da}	−0.680	−0.595	−0.838	1.0	0.835	−0.620	−0.374
ε_{Dm}	−0.545	−0.516	−0.699	0.835	1.0	−0.564	−0.337
ε_{Az}	0.826	0.249	0.680	−0.620	−0.564	1.0	0.288
ε_{Ax}	0.035	0.734	0.545	−0.374	−0.337	0.288	1.0

Table 5. Prediction models of the Box-Cox power λ and the Hurst number H.

λ: a normal variable with mean equal to 0.312 and standard deviation equal to 0.278
H: a value of 0.99 with probability of 0.43 and a normal variable with mean equal to 0.714 and standard deviation equal to 0.172 with probability of 0.57

Next, Fig. 6(a) shows the fault area as a function of M_w. The fault area for the tsunamigenic models is greater than that for the non-tsunamigenic models but their differences are not as remarkable as those for W (Fig. 5(a)). A decrease of the standard deviation of the residuals is noted (Tables 1 and 2). Therefore, a distinction of tsunamigenic and non-tsunamigenic models for the fault area is desirable. The developed relationships are compared with the scaling relationship developed by Murotani *et al.* [2013] [M13]. The comparison indicates that the M13 relationship is in close agreement with the overall scaling relationship (Table 1). Moreover, the ratio between asperity area and fault area S_a/S is useful for constraining stochastic source models [Somerville *et al.*, 1999; Murotani *et al.*, 2013]. Following the definition by Murotani *et al.* [2013], the asperity area S_a is defined as the summed area of subfaults having slips greater than 1.5 times mean slip, and values of S_a/S are evaluated for the 226 source models. Figure 6(b) shows the S_a/S ratio as a function of M_w. The results indicate that the ratio is independent of M_w and does not depend on the data classification. The S_a/S ratio can be modeled as a normal variable with mean equal to 0.240 and standard deviation equal to 0.046. The obtained statistics for the S_a/S ratio are similar to $S_a/S = 0.20$, as suggested by Murotani *et al.* [2013].

3.2.2. *Scaling relationships for slip statistics parameters*

Figure 7 plots the mean slip and maximum slip as a function of M_w. The results for the M_w–D_a relationship clearly show that the data for the tsunamigenic and non-tsunamigenic models are distributed differently; for the same M_w values, D_a for the tsunamigenic events is smaller than D_a for the non-tsunamigenic models. The

differences of the M_w–D_a scaling behavior for the two datasets can be attributed to differences in stress drop for these data (note: mean slip is proportional to stress drop). The statistical analysis carried out by Allmann and Shearer [2009] indicates that stress drop for strike-slip events is 3 to 5 times greater than other types of earthquakes and that stress drop for intra-plate events is 2 times greater than inter-plate events. The non-tsunamigenic models include all strike-slip events and are of intra-plate type, whereas the tsunamigenic models correspond to inter-plate events. Consequently, the stress drop for the non-tsunamigenic models is significantly greater than the stress drop for the tsunamigenic models. Another contributing factor for the differences of D_a values is the fault area (Fig. 6(a)). The M_w–W relationship for the tsunamigenic models is larger than that for the non-tsunamigenic models. Thus the M_w–D_a relationship for the tsunamigenic models is smaller. The results for the M_w–D_m relationship also show different scaling behavior for the tsunamigenic and non-tsunamigenic models.

For D_a, the scaling relationship by Wells and Coppersmith [1994] for all event types as well as the scaling relationship by Murotani *et al.* [2013] is included in Fig. 7. The comparison between the WC94-All relationship and the developed model for the non-tsunamigenic events is consistent, whereas the M13 relationship is in good agreement with the fitted model without model-type distinction (Table 1). These results suggest that the data used in the previous studies may be significantly different, affecting their final scaling relationships. The scaling relationships developed herein are based on much extensive datasets and thus are more robust than the existing scaling models for mean slip. The residuals ε_{Da} and ε_{Dm} are highly correlated; the linear correlation coefficient is about 0.7 to 0.9 (Tables 3 and 4). These correlation coefficients may need to be taken into account when mean and maximum slips are evaluated simultaneously using the developed scaling relationships.

Finally, the scaling behavior of the Box-Cox parameter is examined. Figure 8 shows the M_w–λ relationship. The results indicate that the M_w–λ data points are widely scattered and no clear dependence of λ on M_w is observed. A suitable probability distribution type for λ is the normal distribution. Therefore, the Box-Cox parameter can be modeled as a normal random variable with mean equal to 0.312 and standard deviation equal to 0.278 (Table 5).

3.2.3. *Scaling relationships for spatial slip distribution parameters*

Figures 9(a) and 9(b) show the M_w–A_z and M_w–A_x relationships, respectively. The results indicate that the scaling behavior for A_z differs for the tsunamigenic and non-tsunamigenic events, whereas that for A_x is consistent for the two datasets. The observations are qualitatively similar to W and L (Fig. 5). Further to examine the scaling characteristics of the correlation lengths, correlation lengths normalized by the corresponding source dimensions, i.e. A_z/W and A_x/L, are plotted in Figs. 9(c) and 9(d), respectively, as a function of M_w. The normalized ratio plots, although

they exhibit large variability particularly for the strike direction, show no magnitude- as well as data type-dependency for both down-dip and along-strike directions. In other words, magnitude scaling and data type-dependency of the correlation lengths are similar to those of the source dimensions. This is in agreement with Mai and Beroza [2002].

The obtained relationships are compared in Fig. 9 with the relationships proposed by Mai and Beroza [2002] [MB02]. The comparison suggests that the developed models for the non-tsunamigenic models are similar to the MB02 relationships. Note that the residuals for ε_{Az} and ε_{Ax} are only weakly correlated with the linear correlation coefficient of about 0.3 (Tables 3 and 4). The statistics of the normalized correlation lengths (Figs. 9(c) and 9(d)) are also usable for generating values of A_z and A_x. The mean and standard deviation of the normalized correlation length along dip direction are 0.275 and 0.064, respectively, whereas the mean and standard deviation of the normalized correlation length along strike direction are 0.283 and 0.164, respectively. The lognormal distribution is suitable to model the normalized correlation lengths.

Next, the scaling characteristics of the Hurst number are examined by plotting the M_w–H data pairs in Fig. 10. For many cases (98 out of 226), H is estimated to be 0.99 (upper limit in the parameter estimation) and exhibits large variability when H is less than 0.99. It is noteworthy that H is independent of moment magnitude. Overall, the mean and standard deviation of H are 0.834 and 0.139, respectively, noting that the estimated values of H should be truncated at the upper bound of 0.99. This results in the bimodal distribution of H. Alternatively, H can be modeled as a random variable that takes a value of 0.99 with probability of 0.43 and a sampled value from the normal distribution with mean equal to 0.714 and standard deviation equal to 0.172 with probability of 0.57 (Table 5).

The preceding statistical analysis of the spatial slip distribution parameters has focused on parameters that are estimated based on the manipulated slip distributions (i.e. interpolation and tapering). Variations of these analysis procedures are possible and it is important to assess the sensitivity of the estimated parameters to different analysis settings. For this purpose, three additional spectral analyses are conducted (using the entire set of 226 models): case i considers tapering only (no interpolation); case ii considers interpolation only (no tapering); and case iii considers neither tapering nor interpolation. Comparisons of the estimated spatial slip distribution parameters of the cases i–iii with the base case that considers tapering and interpolation are shown in Fig. 11. Figures 11(a)–11(c) present the effects of interpolation, the effects of tapering, and the combined effects of tapering and interpolation, respectively. The observations that can be made with respect to Fig. 11 are:

- Figure 11(a) shows that the correlation length along dip direction is increased by interpolation, whereas the correlation length along strike direction tends to

be smaller for some models. When the interpolation is not performed, the Hurst number generally increases with respect to the base case. This change is expected as interpolation tends to increase the spectral content in the large wavenumber range, noting that for the von Kármán model the spectral level decays with a slope of $-(H+1)$ (see Eq. (3)). When the interpolation is not considered, the spectral level in the large wavenumber range is decreased and hence a model with a greater H value fits the spectrum better.

- Figure 11(b) shows that the influence on the correlation length along dip direction is not significant, whereas the correlation length along strike direction tends to be greater than the base case for some models. Tapering tends to increase the estimated values of the Hurst number. The increase in the correlation length along strike direction is sometimes very remarkable, resulting in unrealistic estimates of the correlation length. These large values of A_x (unstable results) are often related to small values of $H(< 0.3)$. Although tapering is a manipulation and is not a genuine feature of the original source models, it tends to stabilize the estimation process of the spatial slip distribution parameters.
- Figure 11(c) indicates that the combined effects due to tapering and interpolation lead to similar estimates of A_z, whereas both increase and decrease are observed for A_x. Overall, the estimated values of the Hurst number based on the case without tapering/interpolation are smaller than those for the base case. Some models are affected more strongly by the increased spectral content in the large wavenumber range, while others tend to result in unrealistic estimates of A_x due to small H values.

The results shown in Fig. 11 suggest that the effects due to the manipulations (i.e. tapering and interpolation) on the estimated spatial slip distribution parameters are complex and some models are affected more significantly than others. To examine the impact due to these changes to the scaling relationships, fitted curves for the four cases are compared in Figs. 12(a)–12(c) for the correlation length along dip, the correlation length along strike, and the Hurst number, respectively. For the correlation lengths, the functional form that distinguishes the data types is considered and the fitted curves for the base case are presented together with their confidence intervals (mean plus/minus one standard deviation). It can be observed that for the correlation length along dip direction (Fig. 12(a)), the mean relationships for cases i–iii fall within the confidence intervals of the base case model; the results that do not consider interpolation are greater than other cases (see Fig. 11(a)). On the other hand, for the correlation length along strike direction (Fig. 12(b)), results for all four cases are consistent (note: some anomalous results are observed when the Hurst number is relatively small). These results confirm that overall the scaling relationships of the correlation lengths for the base case are representative of several analysis settings in terms of manipulation of the slip distribution. In contrast to these, the results for the Hurst number (Fig. 12(c)) are more

significantly influenced by the manipulation method. The base case results essentially lie in the middle of the four analysis cases that are considered in this study. Because there is no "correct" way as to how the slip distribution is manipulated prior to spectral analysis, the base case is considered to be adequate in obtaining the source parameters and eventually in developing scaling relationships for these parameters.

3.3. *Limitations of the developed scaling relationships*

The new scaling relationships that are developed in this study offer significant advancement with respect to previous relationships in the literature, notably in the aspects of the comprehensiveness of the multivariate prediction models, which are well suited for implementing them in probabilistic tsunami hazard and risk assessment (Sec. 4). It is important to mention the limitations of the developed prediction models. One limitation is the applicability of the developed models to large mega-thrust subduction earthquakes that may have very long fault rupture zones, exceeding 1000 km (e.g. 2004 Indian Ocean event). Another limitation is related to tsunami earthquakes that are typically characterized by slow rupture processes [Kanamori, 1972; Bell *et al.*, 2014].

The dataset that is used in this study includes three inverted finite-fault rupture models for the 2004 Indian Ocean event; two of the three models have fault lengths exceeding 1000 km [Ammon *et al.*, 2005; Rhie *et al.*, 2007]. These models are at the upper bound of the applicable range of the developed scaling relationships (i.e. M_w9.2) and their effective lengths are above the developed model for the mean plus one standard deviation (Fig. 5(b)). Although the mean plus two standard deviations of the predicted fault length contain such a long fault length, a caution should be exercised in applying the developed prediction models for such extreme situations. In particular, geological and seismological conditions in the source region of interest should be taken into account.

Although the dataset of this study includes several tsunami earthquakes (e.g. 2006 Java event), kinematic features of the earthquake rupture process are not evaluated in this study. For example, to capture the slow rupture process of tsunami earthquakes, rupture propagation velocity and rise time need to be modeled. Unfortunately, the majority of the inverted source models used in this study provide the final spatial slip distributions only and thus are not suitable for such characterizations. In the future, the kinematic source parameters should also be considered in developing a set of scaling relationships.

Additionally, it is known that the ratio of width and length and dip angle have significant impact on tsunami run-up [e.g. Sepúlveda and Liu, 2016]. Although the new M_w–W–L relationships can be directly applied to stochastic tsunami simulation, the dip angle has not yet been characterized. This is a subject of future investigations related to mega-thrust earthquakes.

4. Stochastic Tsunami Simulation Using New Scaling Relationships

In this section, an application of the newly developed scaling relationships (Sec. 3.2) to Monte Carlo tsunami simulation is presented by focusing on locations in the Sendai plain, Miyagi Prefecture, Japan. The sites for tsunami hazard assessment cover coastal areas from Shinchi Town (south) to Sendai City (north) in Miyagi Prefecture (Fig. 13(a)). A source region off the Tohoku region of Japan is defined (Fig. 13(b)), and two scenarios, i.e. M_w8.5 and M_w9.0, are considered. The aim of the investigations is to demonstrate how new prediction models of the source parameters can be implemented in a practical context. Because detailed explanations of the computational method of the Monte Carlo tsunami simulation for particular realizations (without scaling relationships) can be found elsewhere [Goda *et al.*, 2014, 2015; Goda and Abilova, 2016], only brief descriptions of the methodology and data are given in the following.

4.1. *Procedure*

Tsunami hazard assessment can be carried out by implementing a sequence of computations and simulations (Fig. 14). First, earthquake scenarios of interest need to be defined by specifying the moment magnitude, source region/fault model, and asperity zone (Fig. 13(b)). The fault model is developed by referring to the fault plane geometry, such as the location of the trench, top-fault depth, strike, and dip,

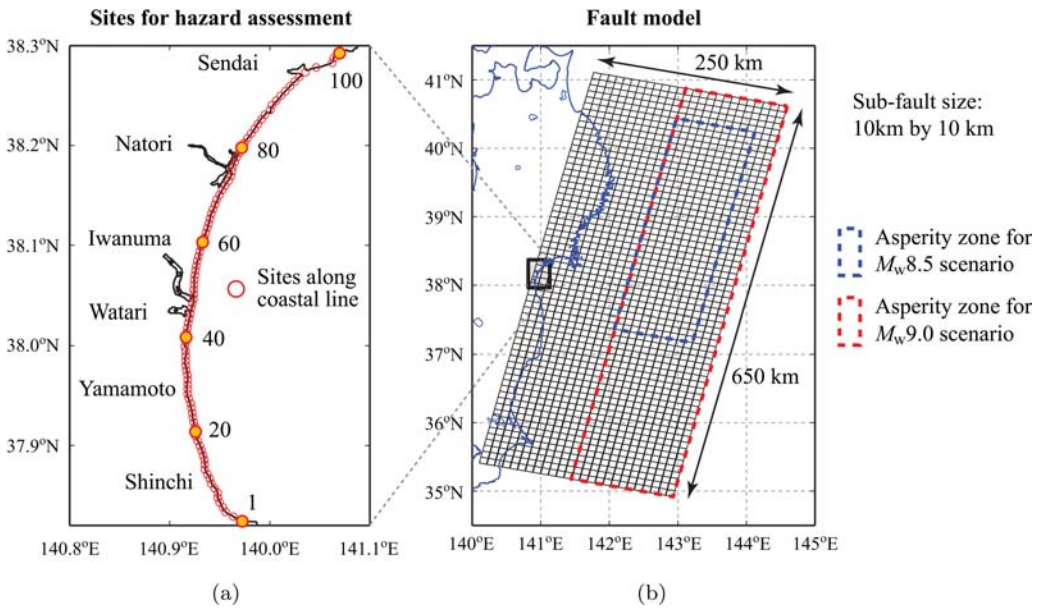

Fig. 13. (a) Selected locations in the Sendai plain, and (b) tsunami source region and fault model off the Tohoku coast of Japan.

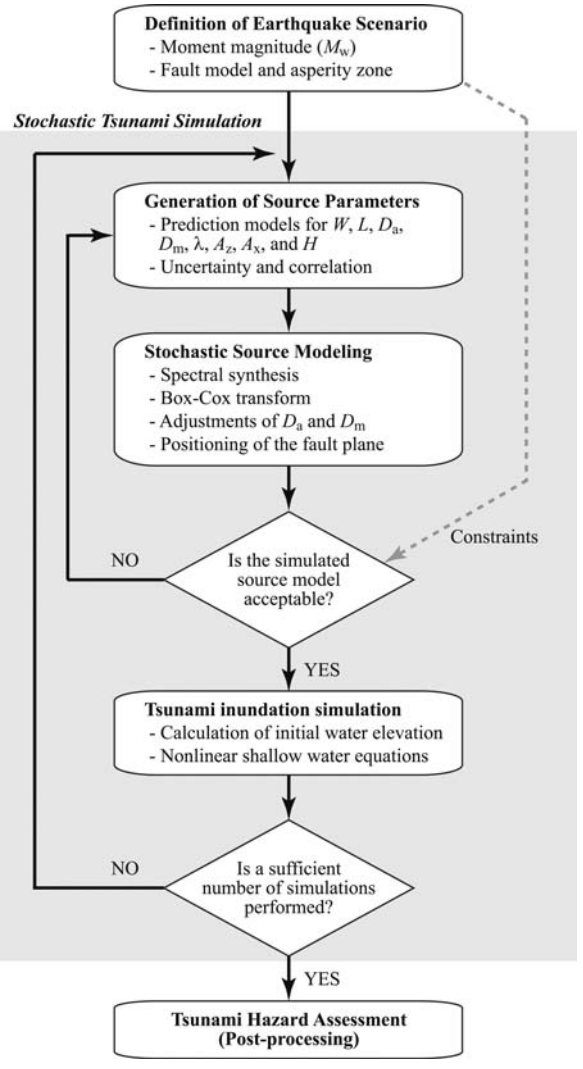

Fig. 14. Analysis procedure for Monte Carlo tsunami simulation using prediction models of earthquake source parameters.

considered by Satake *et al.* [2013]. The fault model, i.e. extended version of the Satake *et al.* fault plane model, covers a 650 km by 250 km area and has a constant strike of 193° and variable dip angles, gradually steepening from 8° to 16° along the down-dip direction. The asperity zone corresponds to a sub-region where a significant amount of earthquake slip is anticipated. In this study, different asperity regions are considered for the M_w8.5 and M_w9.0 scenarios (Fig. 13(b)); the asperity zone for the M_w8.5 scenario is smaller and does not reach the Japan Trench. The adopted scenario parameters essentially reflect the seismological knowledge of earthquake rupture in the target region, which can be adopted as criteria/constraints in determining acceptable synthesized source models.

Second, earthquake source parameters, such as W, L, D_a, D_m, λ, A_z, A_x, and H, are generated using the developed prediction models of these parameters (Tables 1–5). Uncertainties (i.e. prediction errors as characterized by epsilon variables) associated with the regression models should be taken into account in sampling the values of the source parameters. Because some of the regression residuals of the scaling relationships are highly correlated, it is desirable to taken into account the correlation matrix of these residuals to avoid unrealistic combinations of the source parameters (Tables 3 and 4). In the simulation, random numbers for the epsilon variables are sampled from the multivariate standard normal distribution function. Note that λ and H are treated as independent variables.

Third, using the generated spatial slip distribution parameters, a random slip field is generated using a Fourier integral method [Pardo-Iguzquiza and Chica-Olmo, 1993]. To achieve slip distribution with realistic positive skewness, the synthesized slip distribution is converted via Box-Cox transformation [Goda *et al.*, 2014]. The transformed slip distribution is then adjusted to achieve the target mean slip D_a and to avoid very large slip values exceeding the target maximum slip D_m. Subsequently, the position of the synthesized fault plane is determined randomly within the source region. At this stage, consistency among the simulated values of W, L, and D_a can be checked by comparing the target seismic moment (as specified by the scenario magnitude) and the simulated seismic moment ($M_o = \mu W L D_a$, where μ is the rock rigidity and μ is set to 40 GPa; note that a constant rigidity value may not be realistic as this physical quantity changes over depth, see Geist and Bilek [2001]). Due to the variability in W, L, and D_a, random sampling of W, L, and D_a may result in a seismic moment that is very different from the target seismic moment or moment magnitude. To avoid such an inadequate combination of W, L, and D_a, sampling of these three parameters is repeated until the calculated seismic moment falls within a certain range. In this study, the target moment magnitudes minus/plus 0.05 units are considered for such a range.

To ensure that the synthesized slip distribution is realistic with respect to the seismotectonic characteristics of the region, two criteria/constraints are implemented to determine the final acceptance of the generated source model. The first constraint requires that the S_a/S ratio of the candidate slip distribution falls between 0.2 and 0.3 (see Fig. 6(b)). The second constraint requires that the simulated earthquake slip is higher in the designated asperity region. For the 2011 Tohoku earthquake, high concentrations of earthquake slip in the shallow segment of the seismic region (near the Japan Trench) have been suggested by many inversion studies [Goda *et al.*, 2014]. Practically, a candidate slip distribution is accepted if the total slip in the asperity region has a certain slip concentration percentage in terms of total slip across the fault plane. In this study, a slip concentration between 50% and 80% is considered. In the Monte Carlo tsunami simulation, multiple slip distributions are generated repeatedly until an acceptable source model, which has all desirable characteristics, is obtained.

Fourth, for a given acceptable source model, the initial water surface elevation (i.e. initial boundary conditions for tsunami simulation) is evaluated based on formulae by Okada [1985] and Tanioka and Satake [1996]. Tsunami wave propagation is evaluated by solving nonlinear shallow water equations with run-up [Goto *et al.*, 1997]. The computational domains are nested following a 1/3 ratio rule at four resolutions (i.e. 1350, 450, 150, and 50 m domains). A complete dataset of bathymetry/elevation, coastal/riverside structures, and surface roughness is obtained from the Miyagi prefectural government. In the tsunami simulation, the coastal/riverside structures are represented by a vertical wall at one or two sides of the computational cells. To evaluate the volume of water that overpasses these walls, Homma's overflowing formulae are employed. The bottom friction is evaluated using Manning's formula following the Japan Society of Civil Engineers standard [2002]. The fault rupture is assumed to occur instantaneously, and numerical tsunami calculation is performed for duration of 2 h with an integration time step of 0.5 s.

Finally, the above simulation procedure is repeated until a sufficient number of acceptable source models are generated and their tsunami inundation heights/depths at locations of interest are evaluated. The results from the Monte Carlo tsunami simulation are useful for evaluating variability of tsunami simulation results at different locations and for developing stochastic tsunami hazard maps [Goda *et al.*, 2014, 2015].

4.2. *Tsunami hazard results for M_w8.5 and M_w9.0 scenarios*

In the illustrative application, two scenarios, i.e. M_w8.5 and M_w9.0, are considered. In each scenario, two calculation cases are set up; the first case takes into account uncertainties of the scaling relationships (epsilon values in the prediction models are generated; referred to as "with uncertainty" case), while the other case ignores uncertainties of the scaling relationships (epsilon values in the prediction models are set to zero; referred to as "without uncertainty" case). Essentially, the without uncertainty case generates source models with fixed source parameters. The randomness of the synthesized source models is mainly attributed to the stochasticity of the slip distribution (i.e. spectral synthesis) and the uncertainty of the fault plane position within the entire rupture zone. Therefore, even for the without uncertainty case, realizations of the earthquake source models are stochastic. The aim of considering both with uncertainty and without uncertainty cases (with regard to the developed prediction models of the source parameters) is to investigate the effects of prediction errors (epsilon terms) associated with the developed scaling relationships of the source model parameters on tsunami hazard assessment. For each case, 100 Monte Carlo tsunami simulations are conducted (in total, 400 runs are performed).

Figure 15 shows examples of synthesized earthquake source models for the four cases (i.e. M_w8.5 scenario with uncertainty, M_w8.5 scenario without uncertainty,

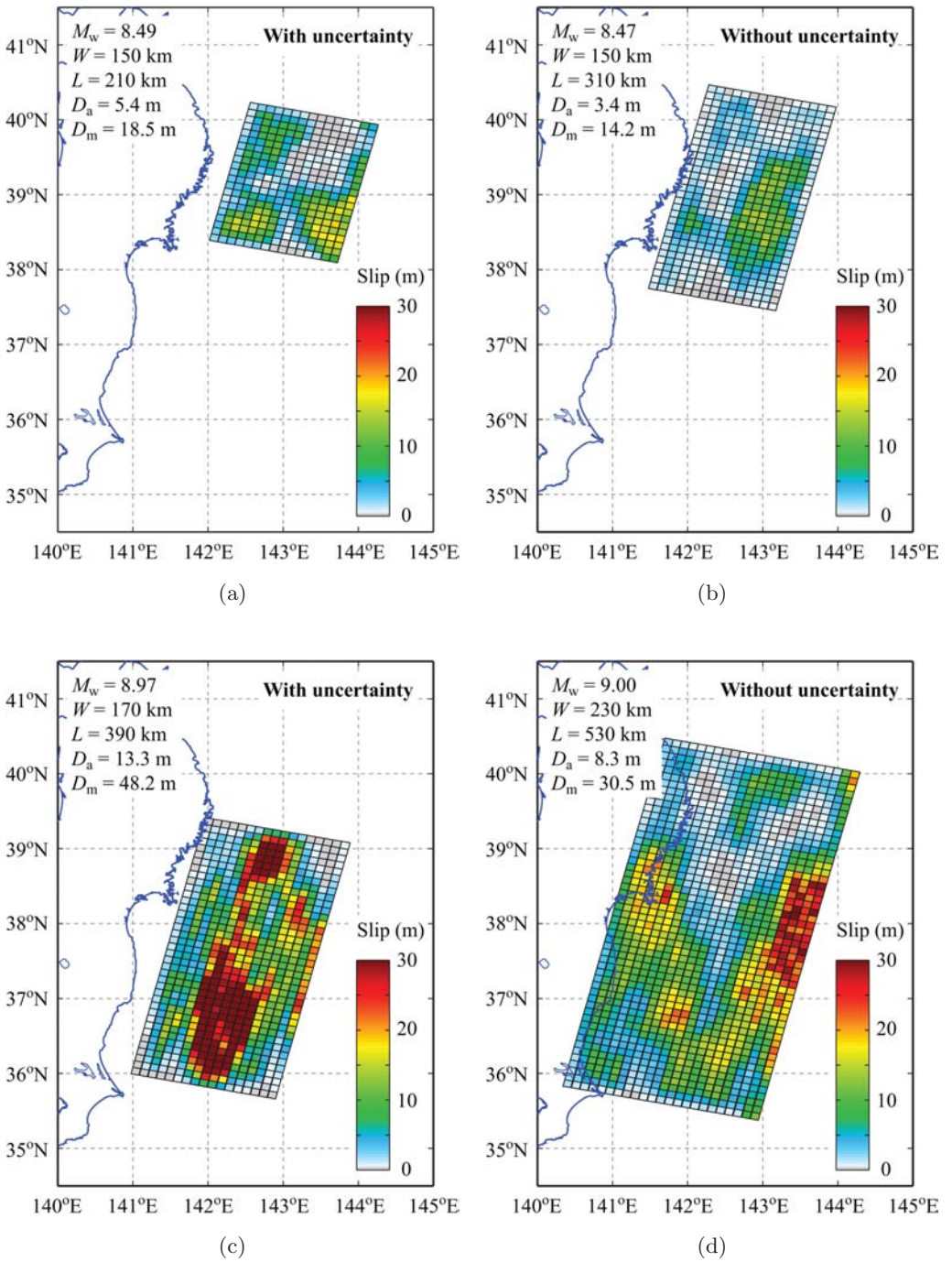

Fig. 15. Examples of synthesized earthquake source models: (a) M_w8.5 scenario (with uncertainty), (b) M_w8.5 scenario (without uncertainty), (c) M_w9.0 scenario (with uncertainty), and (d) M_w9.0 scenario (without uncertainty).

M_w9.0 scenario with uncertainty, and M_w9.0 scenario without uncertainty). Note that the source model shown in the figure is one of the 100 accepted source models, respectively. It can be observed that both fault plane size and slip values increase with moment magnitude, and that the location, size, and extent of the asperity areas also change significantly. The slip values and fault plane size are different for similar moment magnitudes (Fig. 15(a) versus Fig. 15(b), and Fig. 15(c) versus Fig. 15(d)). Through the stochastic synthesis method of random slip fields, various tsunami source characteristics can be taken into account.

Figure 16 shows the variability of the maximum inundation height at 100 locations along the Sendai plain coast (see Fig. 13(a) for the locations of the sites) for the four analysis cases. The elevations at the 100 sites (grid points) along the coast are near zero (within plus/minus 1 m differences). The gray thin lines are the individual simulation results, whereas the blue solid line with circle and the blue broken lines correspond to the median curve and 10th/90th percentile curves of the individual simulation results, respectively. The results indicate that on average the inundation heights increase with earthquake magnitude, and variability of the tsunami heights due to uncertainty of tsunami source characteristics is significant. For the M_w8.5 scenario (Fig. 16(a) versus Fig. 16(b)), the extent of variability (e.g. interval between 10th and 90th percentile curves) is similar for both cases (note: strictly speaking, variability for the with uncertainty case is slightly larger than that for the without uncertainty case; to obtain more robust conclusions, the number of simulations needs to be increased). On the other hand, for the M_w9.0 scenario (Fig. 16(c) versus Fig. 16(d)), a clear tendency for increased variability for the with uncertainty case can be observed. The increase in the variability of tsunami hazard parameters for the with uncertainty case, with respect to the without uncertainty case, is expected because more critical tsunami sources, having smaller fault plane size and more concentrated earthquake slip, can be synthesized as a statistical variation of slip parameters. The results are in agreement with our previous study [Goda *et al.*, 2015] for the fixed fault plane size (i.e. M_w9.0 scenario based on stochastic variations of the Satake *et al.* source model).

Figure 17 displays the probability distribution of inundation area above 3 m depth in the Sendai plain based on 100 simulation results for the four cases. The inundation area above 3 m depth is adopted to define the regional tsunami hazard level by ranking tsunami simulation results, noting that the inundation depth of 3 m corresponds to critical hazard intensity for major destruction of wooden houses [Suppasri *et al.*, 2013]. The inundation hazard curves clearly show that the hazard intensities differ significantly, depending on different scenarios (i.e. M_w8.5 versus M_w9.0). For the M_w9.0 scenario, the inundation hazard curve for the with uncertainty case varies more widely than that for the without uncertainty case; the differences of the hazard curves are particularly large at high probability levels. The uncertainty of the scaling relationships gives significant variation of both lower and upper limits of the probability distribution of the inundation area, although the average inundation

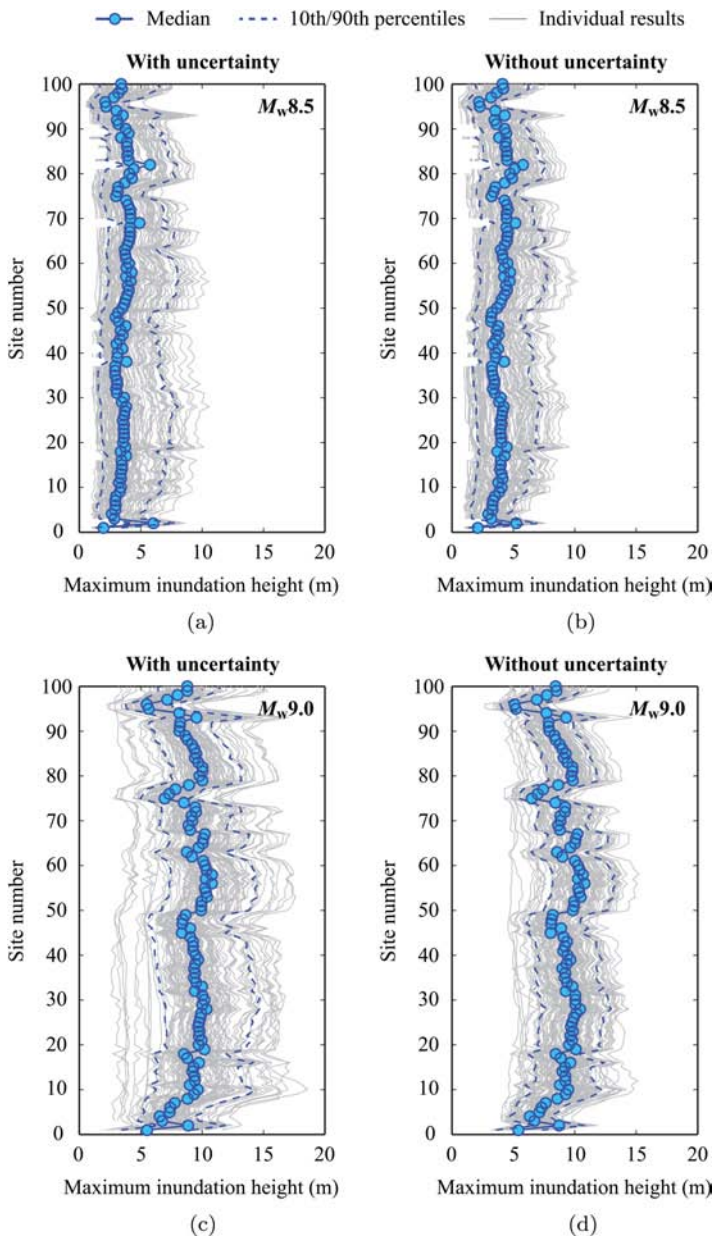

Fig. 16. Variations of tsunami inundation height along the Sendai coast (see Fig. 13(a) for the locations of the sites): (a) $M_w8.5$ scenario (with uncertainty), (b) $M_w8.5$ scenario (without uncertainty), (c) $M_w9.0$ scenario (with uncertainty), and (d) $M_w9.0$ scenario (without uncertainty).

areas are similar. The differences of hazard curves are particularly large at high probability levels; this is particularly useful for evacuation planning because deterministic approaches cannot provide detailed information related to the uncertainty of the hazard estimates for a given scenario.

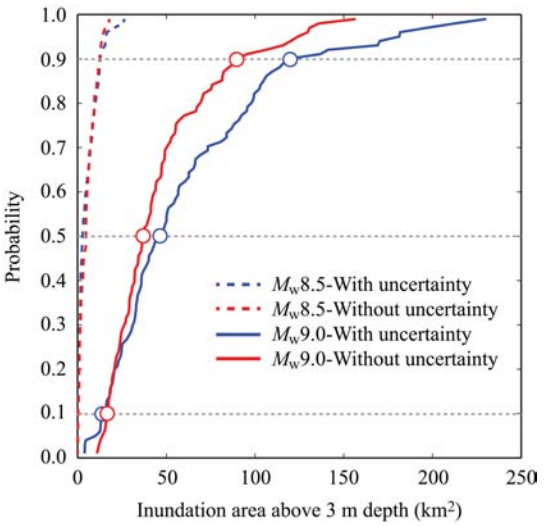

Fig. 17. Probability distribution of inundation area above 3 m depth for four analysis cases.

Moreover, the inundation hazard curves shown in Fig. 17 can be used to define critical tsunami hazard scenarios and inundation maps for the region. Herein, for illustration, three characteristic probability levels, 10th, 50th, and 90th percentiles, are adopted by considering the M_w9.0 scenario. Figures 18 and 19 show probabilistic

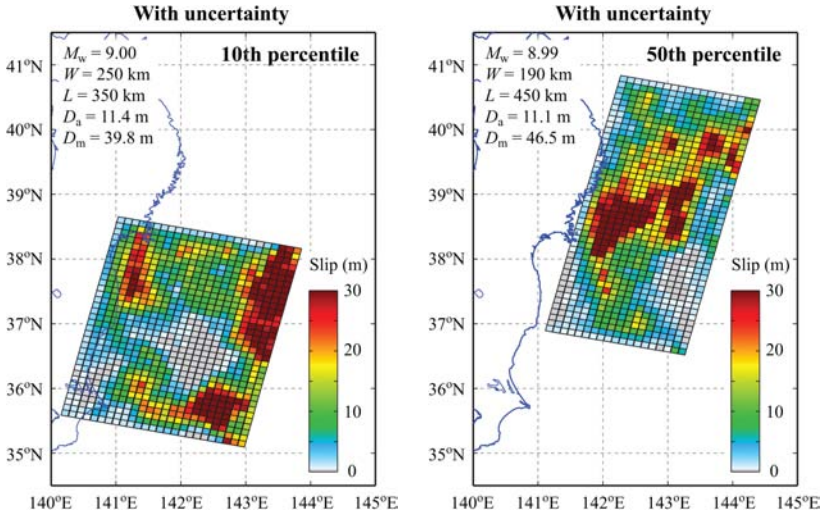

(a) (b)

Fig. 18. Earthquake source models for M_w9.0 scenario determined based on the tsunami hazard curves of inundation area above 3 m depth (Fig. 17): (a) 10th percentile (with uncertainty), (b) 50th percentile (with uncertainty), (c) 90th percentile (with uncertainty), (d) 10th percentile (without uncertainty), (e) 50th percentile (without uncertainty), and (f) 90th percentile (without uncertainty).

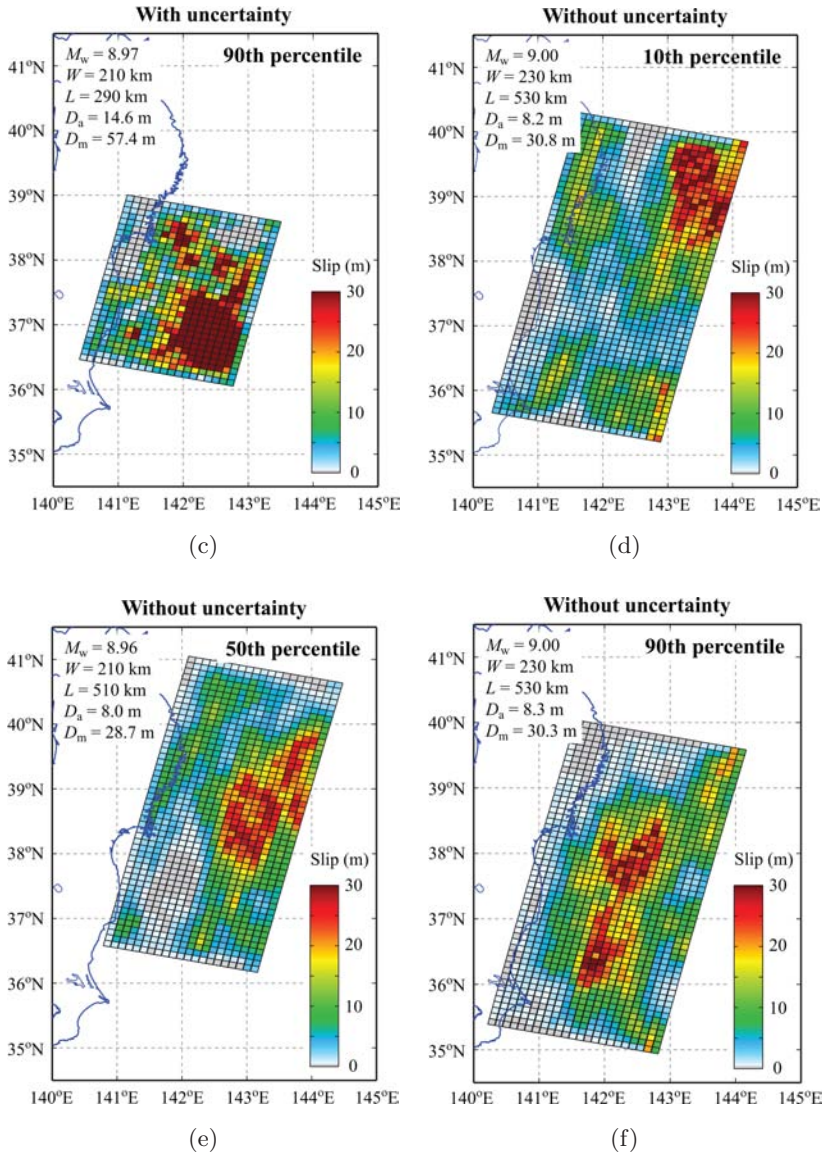

Fig. 18. (*Continued*)

earthquake source models and inundation depth maps, respectively, that correspond to the 10th, 50th, and 90th percentiles of the inundation hazard curves shown in Fig. 17 (indicated by circles). With the increase of the percentile level, more earthquake slip is concentrated near the Sendai plain (Fig. 18), resulting in more severe inundation situations (Fig. 19). Especially, the inundation depth maps for the six cases (Fig. 19) visually show the increase of the tsunami inundation hazard in terms of amplitude and spatial extent. Although the target area, Sendai plain, of this study is smaller than the fault size ($1/3 - 1/5$), the sensitivity of inundation depth

to percentiles is very localized at the scale of $O(10\,\mathrm{km})$. Additionally, the spatial extent of inundation areas with and without uncertainty is similar for the 90th percentiles in Fig. 19, although the inundation depth is different. On the other hand, the spatial extent of inundation areas with and without uncertainty is different for

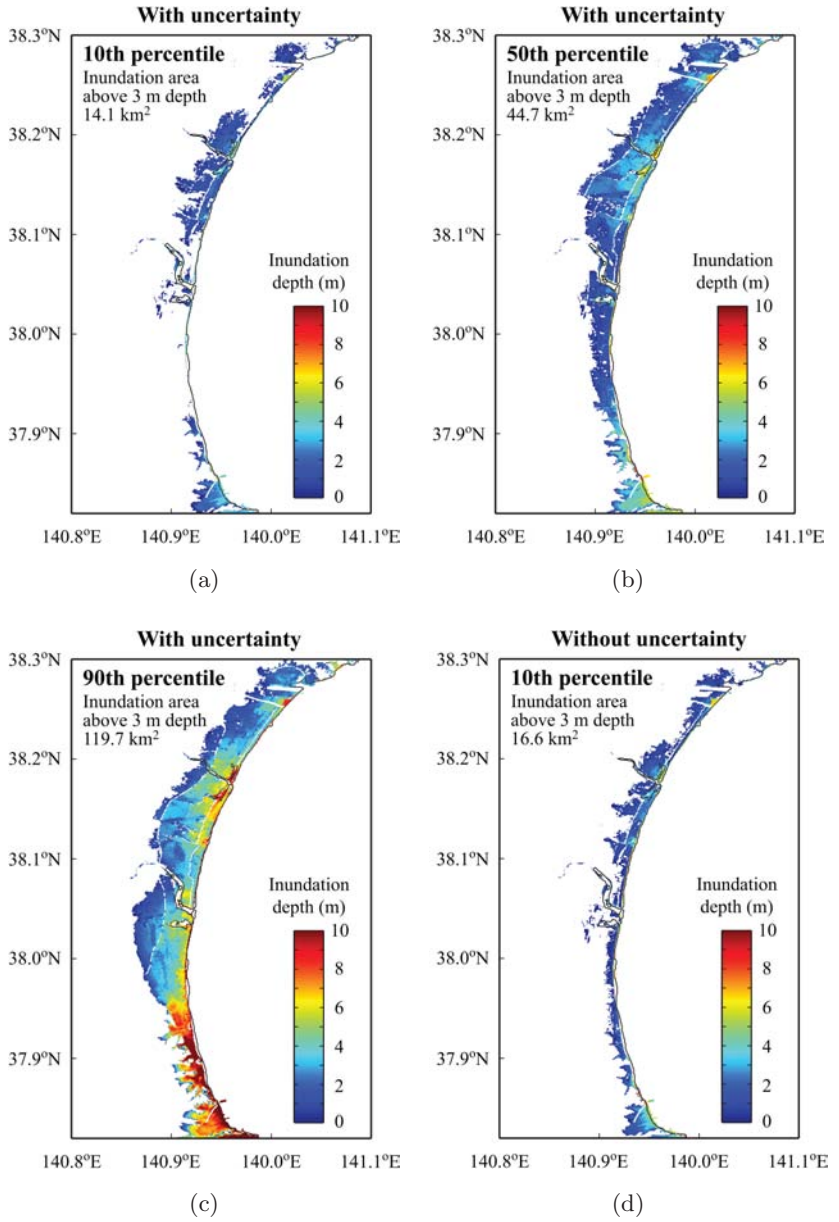

Fig. 19. Inundation depth maps for M_w9.0 scenario determined based on the tsunami hazard curves of inundation area above 3 m depth (Fig. 17): (a) 10th percentile (with uncertainty), (b) 50th percentile (with uncertainty), (c) 90th percentile (with uncertainty), (d) 10th percentile (without uncertainty), (e) 50th percentile (without uncertainty), and (f) 90th percentile (without uncertainty).

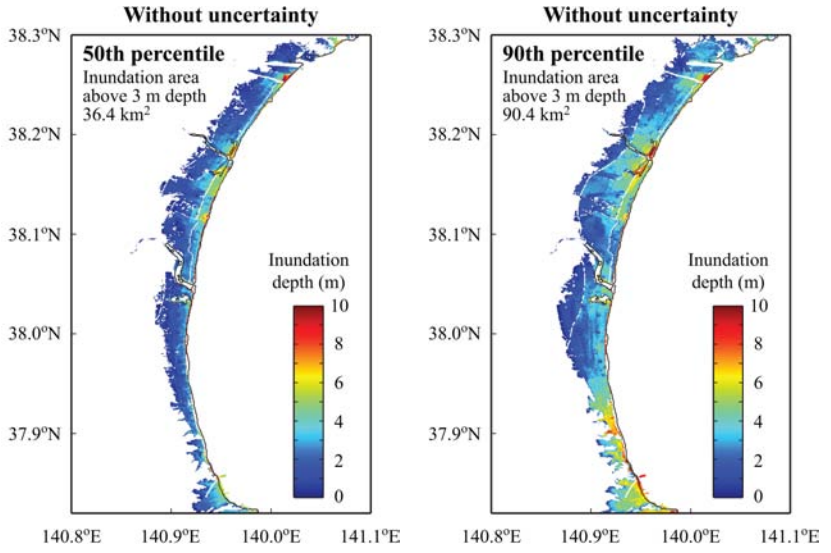

Fig. 19. (*Continued*)

the 10th percentiles. Both upper and lower sides of inundation extent and depth give information regarding vulnerable areas and their sensitivity/variability in tsunami hazard assessment.

5. Conclusions

In this paper, new scaling relationships of earthquake source parameters were developed using the extensive set of 226 finite-fault rupture models obtained from the SRCMOD database to fill the critical research gap in stochastic earthquake source modeling. The novelty and significance of this study are that the new models consider not only geometry and slip parameters but also spatial slip distribution parameters, and can be implemented as multivariate prediction models in probabilistic tsunami hazard and risk assessment. The underlying rupture models covered a wide range of earthquake magnitudes (from M_w5.8 to M_w9.2) and earthquake types (strike-slip/reverse/normal as well as tsunamigenic/non-tsunamigenic). The considered source parameters included the fault width, fault length, fault area, mean slip, maximum slip, Box-Cox power, correlation lengths along-dip and along-strike directions, and Hurst number. These source parameters were uniformly and consistently estimated through effective dimension analysis, Box-Cox analysis, and spectral analysis.

The scaling relationships of the source parameters were developed through regression analysis by considering the entire dataset and by distinguishing tsunamigenic and non-tsunamigenic models. The results indicated that the distinction between tsunamigenic and non-tsunamigenic data was beneficial for the fault width,

mean slip, and along-dip correlation length in reducing the regression errors associated with the scaling relationships. The reason for different scaling behaviors of the width-related parameters was because the fault planes of the tsunamigenic models dip more gently than those of the non-tsunamigenic models and thus can be extended more toward the down-dip direction than the non-tsunamigenic models. Comparison of the developed scaling relationships with existing relationships indicated that the new models were generally consistent with the existing ones for magnitudes less than 8.0, whereas significantly different scaling relationships were obtained for M_w8.0–9.0 mega-thrust events. The differences of the scaling models can be attributed to the differences of the underlying data. The previous relationships did not have many data points for large subduction events, whereas this aspect has been significantly improved in this study by adopting the extensive SRCMOD database.

To demonstrate how the developed scaling relationships can be implemented in stochastic tsunami simulation, numerical cases were set up by focusing on locations in the Sendai plain, Miyagi, Japan, and two earthquake scenarios (M_w8.5 and M_w9.0). A computational flowchart was provided as practical guidance for the analysis procedure. As part of the demonstration, the effects of variable source parameters due to uncertainties of the scaling relationships (for a given moment magnitude) on tsunami hazard parameters were investigated. The results highlighted that the impact of accounting for randomness in source parameter generation had major influence on local tsunami hazard parameters and thus such uncertainties should be considered in probabilistic tsunami hazard and risk assessment.

As a final remark, although the new scaling relationships of earthquake source parameters and their applications were discussed in the context of tsunami hazard analysis, the developed models should also be applicable to ground motion simulation.

Data Availability

The values of the earthquake source model parameters that are used for developing the prediction models are available from doi: 10.5523/bris.s4tnp1cbdr741h3b63ic10zq5. The computer codes (MATLAB language) for stochastic source modeling may be available on a case-by-case basis.

Acknowledgments

The bathymetry and elevation data for the Tohoku region were provided by the Miyagi prefectural government. This work was supported by the Engineering and Physical Sciences Research Council (EP/M001067/1). The authors are grateful to Martin Mai and Kiran Thingbaijam for insightful discussions on the earthquake source modeling. The authors thank Anawat Suppasri (handling editor) and three anonymous reviewers for their constructive suggestions to improve the manuscript.

References

Allmann, B. P. & Shearer, P. M. [2009] "Global variations of stress drop for moderate to large earthquakes," *J. Geophys. Res. Solid Earth* **114**, B01310, doi:10.1029/2008JB005821.

Ammon, C. J., Chen, J., Thio, H. K., Robinson, D., Ni, S., Hjorleifsdottir, V., Kanamori, H., Lay, T., Das, S., Helmberger, D., Ichinose, G., Polet, J. & Wald, D. [2005] "Rupture process of the great 2004 Sumatra-Andaman earthquake," *Science* **308**, 1133–1139.

Anguiano, E., Pincorbo, M. & Aguilar, M. [1993] "Fractal characterization by frequency analysis I: Surfaces," *J. Microscopy* **172**, 223–232.

Bell, R., Holden, C., Power, W., Wang, X. & Downes, G. [2014] "Hikurangi margin tsunami earthquake generated by slow seismic rupture over a subducted seamount," *Earth Planet. Sci. Lett.* **397**, 1–9.

Beresnev, I. A. [2003] "Uncertainties in finite-fault slip inversions: To what extent to believe?" *Bull. Seismol. Soc. Am.* **93**, 2445–2458.

Blaser, L., Kruger, F., Ohrnberger, M. & Scherbaum, F. [2010] "Scaling relations of earthquake source estimates with special focus on subduction environment," *Bull. Seismol. Soc. Am.* **106**, 2914–2926.

Davies, G., Horspool, N. & Miller, V. [2015] "Tsunami inundation from heterogeneous earthquake slip distributions: Evaluation of synthetic source models," *J. Geophys. Res. Solid Earth* **120**, 6431–6451.

Fukutani, Y., Suppasri, A. & Imamura, F. [2015] "Stochastic analysis and uncertainty assessment of tsunami wave height using a random source parameter model that targets a Tohoku-type earthquake fault," *Stoch. Environ. Res. Risk Assess.* **29**, 1763–1779.

Geist, E. L. [2002] "Complex earthquake rupture and local tsunamis," *J. Geophys. Res. Solid Earth* **107**, ESE 2-1–ESE 2-15.

Geist, E. L. & Bilek, S. L. [2001] "Effect of depth-dependent shear modulus on tsunami generation along subduction zones," *Geophys. Res. Lett.* **28**, 1315–1318.

Goda, K. & Abilova, K. [2016] "Tsunami hazard warning and risk prediction based on inaccurate earthquake source parameters," *Nat. Haz. Earth Syst. Sci.* **16**, 577–593.

Goda, K., Mai, P. M., Yasuda, T. & Mori, N. [2014] "Sensitivity of tsunami wave profiles and inundation simulations to earthquake slip and fault geometry for the 2011 Tohoku earthquake," *Earth Planet. Space* **66**, 105, doi:10.1186/1880-5981-66-105.

Goda, K., Yasuda, T., Mori, N. & Mai, P. M. [2015] "Variability of tsunami inundation footprints considering stochastic scenarios based on a single rupture model: Application to the 2011 Tohoku earthquake," *J. Geophys. Res. Oceans* **120**, 4552–4575.

Goto, C., Ogawa, Y., Shuto, N. & Imamura, F. [1997] "Numerical method of tsunami simulation with the leap-frog scheme," IOC Manual, UNESCO, No. 35, Paris, France.

Horspool, N., Pranantyo, I., Griffin, J., Latief, H., Natawidjaja, D. H., Kongko, W. & Thio, H. K. [2014] "A probabilistic tsunami hazard assessment for Indonesia," *Nat. Haz. Earth Sys. Sci.* **14**, 3105–3122.

Hyndman, R. D. & Wang, K. [1995] "The rupture zone of Cascadia great earthquakes from current deformation and the thermal regime," *J. Geophys. Res. Solid Earth* **100**, 22133–22154.

Japan Society of Civil Engineers [2002] "Tsunami assessment method for nuclear power plants in Japan," Available at: https://www.jsce.or.jp/committee/ceofnp/Tsunami/eng/JSCE_Tsunami_060519.pdf.

Kanamori, H. [1972] "Mechanism of tsunami earthquakes," *Phys. Earth Planet. Inter.* **6**, 346–359.

Lavallée, D., Liu, P. & Archuleta, R. J. [2006] "Stochastic model of heterogeneity in earthquake slip spatial distributions," *Geophys. J. Int.* **165**, 622–640.

Leonard, M. [2010] "Earthquake fault scaling: Self-consistent relating of rupture length, width, average displacement, and moment release," *Bull. Seismol. Soc. Am.* **100**, 1971–1988.

Løvholt, F., Pedersen, G., Bazin, S., Kuhn, D., Bredesen, R. E. & Harbitz, C. [2012] "Stochastic analysis of tsunami runup due to heterogeneous coseismic slip and dispersion," *J. Geophys. Res.* **117**, C03047.

Mai, P. M. & Beroza, G. C. [2000] "Source scaling properties from finite-fault-rupture models," *Bull. Seismol. Soc. Am.* **90**, 604–615.

Mai, P. M. & Beroza, G. C. [2002] "A spatial random field model to characterize complexity in earthquake slip," *J. Geophys. Res. Solid Earth* **107**, ESE 10-1–ESE 10-21.

Mai, P. M. & Thingbaijam, K. K. S. [2014] "SRCMOD: An online database of finite-fault rupture models," *Seismol. Res. Lett.* **85**, 1348–1357.

Mueller, C., Power, W. L., Fraser, S. & Wang, X. [2015] "Effects of rupture complexity on local tsunami inundation: Implications for probabilistic tsunami hazard assessment by example," *J. Geophys. Res. Solid Earth* **120**, 488–502.

Murotani, S., Satake, K. & Fujii, Y. [2013] "Scaling relations of seismic moment, rupture area, average slip, and asperity size for M9 subduction-zone earthquakes," *Geophys. Res. Lett.* **40**, 5070–5074.

Okada, Y. [1985] "Surface deformation due to shear and tensile faults in a half-space," *Bull. Seismol. Soc. Am.* **75**, 1135–1154.

Papazachos, B. C., Scordilis, E. M., Panagiotopoulos, D. G., Papazachos C. B. & Karakaisis, G. F. [2004] "Global relations between seismic fault parameters and moment magnitude of earthquakes," *Bull. Geol. Soc. Greece* **36**, 1482–1489.

Pardo-Iguzquiza, E. & Chica-Olmo, M. [1993] "The Fourier integral method: An efficient spectral method for simulation of random fields," *Math. Geol.* **25**, 177–217.

Rhie, J., Dreger, D., Burgmann, R. & Romanowicz, B. [2007] "Slip of the 2004 Sumatra–Andaman earthquake from joint inversion of long-period global seismic waveforms and GPS static offsets," *Bull. Seismol. Soc. Am.* **97**, S115–S127.

Satake, K., Fujii, Y., Harada, T. & Namegaya, Y. [2013] "Time and space distribution of coseismic slip of the 2011 Tohoku earthquake as inferred from tsunami waveform data," *Bull. Seismol. Soc. Am.* **103**, 1473–1492.

Sepúlveda, I. & Liu, P. L. F. [2016] "Estimating tsunami runup with fault plane parameters," *Coastal Eng.* **112**, 57–68.

Somerville, P., Irikura, K., Graves, R., Sawada, S., Wald, D., Abrahamson, N., Iwasaki, Y., Kagawa, T., Smith, N. & Kowada, A. [1999] "Characterizing crustal earthquake slip models for the prediction of strong ground motion," *Seismol. Res. Lett.* **70**, 59–80.

Strasser, F., Arango, M. & Bommer, J. J. [2010] "Scaling of the source dimensions of interface and intraslab subduction-zone earthquakes with moment magnitude," *Seismol. Res. Lett.* **81**, 941–950.

Suppasri, A., Mas, E., Charvet, I., Gunasekera, R., Imai, K., Fukutani, Y., Abe, Y. & Imamura, F. [2013] "Building damage characteristics based on surveyed data and fragility curves of the 2011 Great East Japan tsunami," *Nat. Haz.* **66**, 319–341.

Tanioka Y. & Satake, K. [1996] "Tsunami generation by horizontal displacement of ocean bottom," *Geophys. Res. Lett.* **23**, 861–864.

Thingbaijam, K. K. S. & Mai, P. M. [2016] "Evidence for truncated exponential probability distribution of earthquake slip," *Bull. Seismol. Soc. Am.* **106**, 1802–1816.

Tsujio, D., Goda, K., Yasuda, T. & Mori, N. [2015] "Sensitivity analysis on breakwater stability of tsunami uncertainty by stochastic tsunami source model for Tohoku earthquake," *J. Japan Soc. Civil Eng. Ser. B2* (*Coastal Eng.*) **71**, 895–900.

Wells, D. L. & Coppersmith, K. J. [1994] "New empirical relationships among magnitude, rupture length, rupture width, rupture area, and surface displacement," *Bull. Seismol. Soc. Am.* **84**, 974–1002.

Ye, L., Lay, T., Kanamori, H. & Rivera, L. [2016] "Rupture characteristics of major and great ($M_w \geq$ 7.0) megathrust earthquakes from 1990–2015: I. Source parameter scaling relationships," *J. Geophys. Res. Solid Earth* **121**, 826–844.